



NRL/MR/5651--17-9731

Investigation of Noise in Photonic Links and Components

MATTHEW J. MONDICH

*Photonics Technology Branch
Optical Sciences Division*

MEREDITH N. HUTCHINSON

*Optical Techniques Branch
Optical Sciences Division*

October 24, 2017

Approved for public release; distribution is unlimited.

REPORT DOCUMENTATION PAGE				Form Approved OMB No. 0704-0188	
Public reporting burden for this collection of information is estimated to average 1 hour per response, including the time for reviewing instructions, searching existing data sources, gathering and maintaining the data needed, and completing and reviewing this collection of information. Send comments regarding this burden estimate or any other aspect of this collection of information, including suggestions for reducing this burden to Department of Defense, Washington Headquarters Services, Directorate for Information Operations and Reports (0704-0188), 1215 Jefferson Davis Highway, Suite 1204, Arlington, VA 22202-4302. Respondents should be aware that notwithstanding any other provision of law, no person shall be subject to any penalty for failing to comply with a collection of information if it does not display a currently valid OMB control number. PLEASE DO NOT RETURN YOUR FORM TO THE ABOVE ADDRESS.					
1. REPORT DATE (DD-MM-YYYY) 24-10-2017		2. REPORT TYPE Memorandum		3. DATES COVERED (From - To) 01 January 2016 – 31 December 2016	
4. TITLE AND SUBTITLE Investigation of Noise in Photonic Links and Components				5a. CONTRACT NUMBER	
				5b. GRANT NUMBER	
				5c. PROGRAM ELEMENT NUMBER NCRADA-NRL-14-552	
6. AUTHOR(S) Matthew J. Mondich and Meredith N. Hutchinson				5d. PROJECT NUMBER	
				5e. TASK NUMBER	
				5f. WORK UNIT NUMBER 6A65	
7. PERFORMING ORGANIZATION NAME(S) AND ADDRESS(ES) Naval Research Laboratory 4555 Overlook Avenue, SW Washington, DC 20375-5320				8. PERFORMING ORGANIZATION REPORT NUMBER NRL/MR/5651--17-9731	
9. SPONSORING / MONITORING AGENCY NAME(S) AND ADDRESS(ES) Office of Naval Research One Liberty Center 875 North Randolph Street, Suite 1425 Arlington, VA 22203-1995				10. SPONSOR / MONITOR'S ACRONYM(S) ONR	
				11. SPONSOR / MONITOR'S REPORT NUMBER(S)	
12. DISTRIBUTION / AVAILABILITY STATEMENT Approved for public release; distribution is unlimited.					
13. SUPPLEMENTARY NOTES					
14. ABSTRACT Sources of excess noise in photonic links and components that originate in the optical domain and manifest as low-frequency noise in the radio-frequency (RF) domain were studied: double Rayleigh scattering-induced relative intensity noise and component-induced phase noise. Techniques to reduce excess noise, such as optimization of link architecture, component biases, and DC photocurrent levels were applied. Fiber-based optoelectronic oscillators were built and characterized, one of which incorporated a method to potentially minimize close-in RF phase noise that entailed using the phase noise impressed on one continuous-wave laser wavelength to cancel that impressed on another.					
15. SUBJECT TERMS Fiber-optics Relative intensity noise RF photonics Phase noise Analog photonics Optoelectronic oscillators					
16. SECURITY CLASSIFICATION OF:			17. LIMITATION OF ABSTRACT Unclassified Unlimited	18. NUMBER OF PAGES 44	19a. NAME OF RESPONSIBLE PERSON Matthew Mondich
a. REPORT Unclassified Unlimited	b. ABSTRACT Unclassified Unlimited	c. THIS PAGE Unclassified Unlimited			19b. TELEPHONE NUMBER (include area code) (202) 767-5370

Table of Contents

1	Executive Summary.....	1
2	Introduction.....	2
3	Experiment 1: Techniques to Address Noise Due to Double Rayleigh Scattering.....	3
4	Experiment 2: Techniques to Reduce Phase Noise in the RF Domain.....	11
5	Experiment 3: Fiber-Based Optoelectronic Oscillators.....	19
	Appendix A Instrumentation & Components.....	27
	Appendix B Calculation of DC Photocurrent.....	31
	Appendix C Output Noise Power Spectral Density & Relative Intensity Noise.....	33
	References.....	39

List of Tables

Table 4.1: Variants of the link evaluated during the residual phase noise tests.....	15
Table 4.2: Test matrix showing executed residual phase noise tests.....	15
Table 5.1: Results of measurements taken on the three OEO structures.....	24
Table A.1: Laboratory instrumentation used during experiment 1.....	27
Table A.2: Laboratory instrumentation used during experiment 2.....	27
Table A.3: Laboratory instrumentation used during experiment 3.....	27
Table A.4: Link components used during experiment 1.....	28
Table A.5: Link components used during experiment 2.....	29
Table A.6: Link components used in experiment 3.....	30

List of Figures

Fig. 3.1: Link with polarization multiplexing/de-multiplexing and balanced detection.....	3
Fig. 3.2: Link with polarization multiplexing/de-multiplexing, retroreflection, and balanced detection.....	4
Fig. 3.3: Optical RIN spectrum for link utilizing polarization multiplexing/de-multiplexing and balanced detection to reduce noise due to DRS.....	8
Fig. 3.4: Optical RIN spectrum for link utilizing polarization multiplexing/de-multiplexing, balanced detection, and retroreflection to address noise due to DRS.....	10
Fig. 4.1: Absolute phase noise measurement setup.....	12
Fig. 4.2: Residual phase noise measurement setup.....	12
Fig. 4.3: Measured SSB phase noise spectra for the four absolute phase noise tests.....	14
Fig. 4.4: Measured SSB phase noise spectra for the residual phase noise tests conducted with two 25 km spools of SMF.....	16
Fig. 4.5: Measured SSB phase noise spectra for the residual phase noise tests conducted with one 25 km spool of SMF.....	17
Fig. 4.6: Comparison of measured SSB phase noise from all eight residual phase noise tests...	18
Fig. 5.1: Generic OEO with a 2 km span of SMF.....	20
Fig. 5.2: OEO utilizing a FRM to produce retroreflection, which effectively doubles the length of the 2 km span of SMF shown.....	20
Fig. 5.3: OEO with proposed RF phase noise cancellation scheme.....	21
Fig. 5.4: Measured SSB phase noise spectra of OEO with RF phase noise cancellation.....	25
Fig. B.1: Diagram used to calculate and equalize photodiode A & B DC photocurrents.....	31
Fig. C.1: Single-sided output noise power spectral density (PSD) for entire link utilizing polarization multiplexing/de-multiplexing and balanced detection to reduce noise due to DRS.	33
Fig. C.2: Single-sided output noise power spectral density (PSD) for optical section of link utilizing polarization multiplexing/de-multiplexing and balanced detection to reduce noise due to DRS.....	34
Fig. C.3: Single-sided output noise power spectral density (PSD) for entire link utilizing polarization multiplexing/de-multiplexing, balanced detection, and retroreflection to address noise due to DRS.....	35
Fig. C.4: Single-sided output noise power spectral density (PSD) for optical section of link utilizing polarization multiplexing/de-multiplexing, balanced detection, and retroreflection to address noise due to DRS.....	36

1 Executive Summary

Work was executed during calendar year 2016 by the Naval Research Laboratory, Applied RF Photonics Section, Code 5651. This work entailed the study of detrimental sources of optical noise and propagation effects that give rise to low-frequency noise in the radio-frequency (RF) domain; application of techniques in the optical domain to mitigate these impairments; and the construction and characterization of fiber-based optoelectronic oscillators (OEOs), one of which has an incorporated technique to potentially minimize close-in RF phase noise.

Three experiments were conducted to accomplish the aforesaid work. The first entailed investigating two techniques to address low-frequency noise in the RF domain due to double Rayleigh scattering (DRS)-induced relative intensity noise (RIN) in the optical domain. The second involved investigation of techniques to reduce close-in phase noise in the RF domain by optimization of link architecture, component biases, and DC photocurrent levels. The third consisted of building three OEO structures, one of which included two continuous-wave lasers at different wavelengths, and investigating whether RF phase noise impressed on one laser wavelength could be used to cancel that impressed on the other to minimize close-in phase noise in the RF domain.

One of the two investigated techniques to address low-frequency noise in the RF domain due to DRS-induced RIN was effective at minimizing noise in the RF domain (polarization multiplexing/de-multiplexing with balanced detection) and the other was not (polarization multiplexing/de-multiplexing with retroreflection and balanced detection).

Close-in RF phase noise was minimized by constructing a link with as short a fiber span as practical without the use of a dispersion compensating module, operating the photodiode and low-phase noise amplifier in the link at their highest allowable voltages, and operating the link at an optical power level that yields moderate DC photocurrent.

The RF phase noise of the OEO structure with the two different wavelength lasers was measured. However, it could not be determined whether phase noise impressed on one wavelength could be used to cancel that on another due to two RF components being out of specification, which caused the relative RF phase between the two paths in the setup, each containing a different wavelength laser, to be incorrectly set. Recommend redoing the measurements at a later date with RF components that are within specification.

2 Introduction

During calendar year 2016 work was conducted by the Naval Research Laboratory, Applied RF Photonics Section, Code 5651. This work consisted of three parts: the study of sources of excess noise and deleterious propagation effects in the optical domain that manifest as low-frequency noise in the radio-frequency (RF) domain; application of techniques to address the detrimental optical noise and propagation effects; and the construction and characterization of fiber-based optoelectronic oscillators (OEO), one of which has an implemented technique to potentially minimize close-in RF phase noise.

A series of three experiments were conducted to accomplish the aforementioned work.

Experiment 1: Techniques to address noise due to double Rayleigh scattering (DRS)

- Polarization multiplexing/de-multiplexing with balanced detection
- Polarization multiplexing/de-multiplexing with retroreflection and balanced detection

Experiment 2: Techniques to reduce phase noise in the RF domain

- Varying photodiode bias voltage, low-phase noise amplifier bias voltage, and DC photocurrent
- Fixed photodiode bias voltage, low-phase noise amplifier bias voltage, and DC photocurrent with the use of a dispersion compensating module (DCM)

Experiment 3: Fiber-based OEOs

- Generic OEO
- OEO with retroreflection
- OEO with RF phase noise cancellation scheme

The following sections detail the aspects of these experiments, which include the following: purpose, objectives, experimental setup, results & discussion, and conclusions & recommendations.

3 Experiment 1: Techniques to Address Noise Due to Double Rayleigh Scattering

Two approaches were taken in an attempt to reduce noise in the RF domain due to DRS: polarization multiplexing/de-multiplexing with balanced detection, and the aforementioned with retroreflection.

3.1 Purpose

This experiment, with the above two approaches implemented, was conducted to:

- Determine whether low-frequency noise in the RF domain due to DRS-induced relative intensity noise (RIN) in the optical domain could be reduced.

3.2 Objectives

The goals of this experiment were as follows:

- Reduce low-frequency noise in the RF domain due to RIN in the optical domain arising from DRS.
- Determine whether RIN due to DRS is polarization dependent.

3.3 Experimental Setup

Setup diagrams of the two implemented approaches to reduce noise due to DRS are shown in Figs. 3.1-3.2. Laboratory instrumentation and link components shown in the figures are listed in Tables A.1 and A.4 in Appendix A.

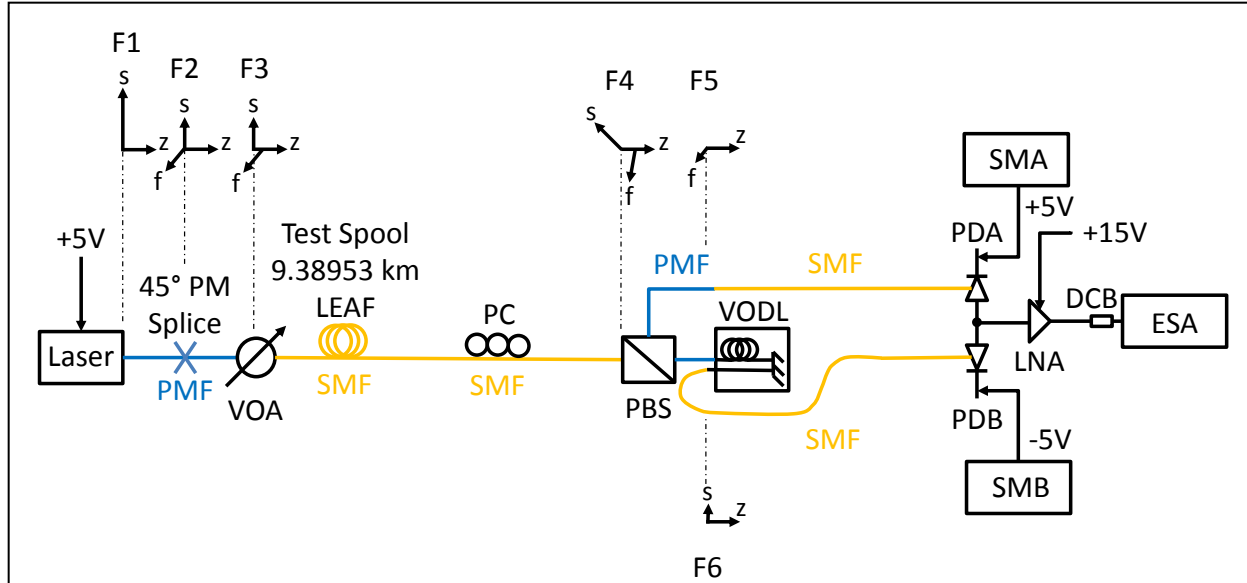


Fig. 3.1: Link with polarization multiplexing/de-multiplexing and balanced detection. F1-F6: reference frames 1 through 6; s: slow axis; f: fast axis; and z: direction of propagation. The linewidth of the continuous-wave (CW) laser is 119 kHz; the stimulated Brillouin scattering

(SBS) threshold and attenuation coefficient of the test spool are 9.00 dBm and 0.24 dB/km, respectively; the average small-signal gain and noise figure of the low noise amplifier (LNA) are 45.6 dB and 1.5 dB, respectively; and the responsivities of photodiodes A and B are 0.73 A/W and 0.71 A/W, respectively. All of these performance parameters were measured.

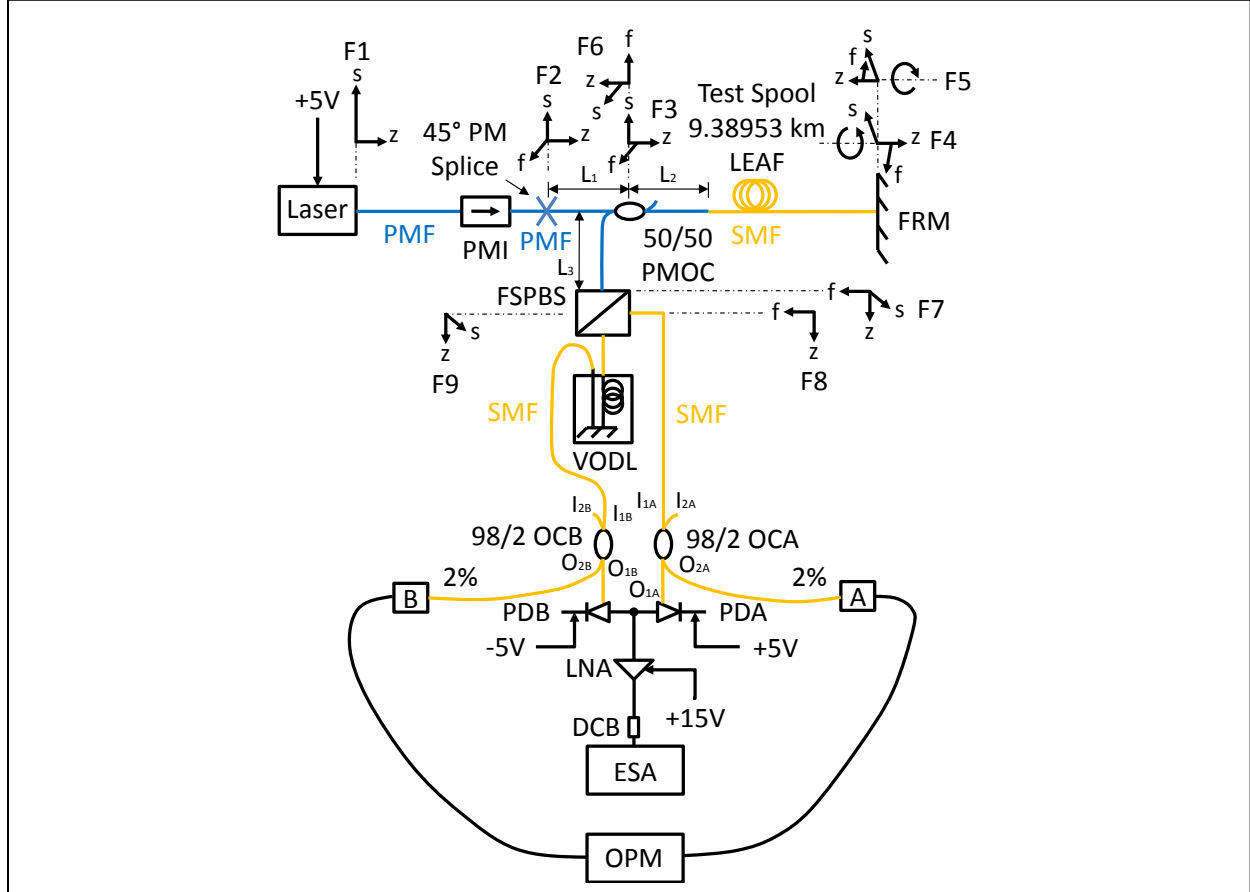


Fig. 3.2: Link with polarization multiplexing/de-multiplexing, retroreflection, and balanced detection. L_1 - L_3 : lengths of polarization-maintaining fiber (PMF); I_{1A} , I_{2A} , I_{1B} , & I_{2B} : inputs to optical couplers A & B; O_{1A} , O_{2A} , O_{1B} , & O_{2B} : outputs of optical couplers A & B.

A description of the setups shown in Figs. 3.1-3.2 is provided in the following four paragraphs.

From the output of the CW laser up through detection with the balanced detector, the following occurred with respect to the propagating light in Fig. 3.1. Light emitted by the laser was launched along the slow axis of the attached PMF, contacted the 45° polarization-maintaining (PM) splice, and was evenly split between the slow and fast principal polarization axes. The intensity of the light was then attenuated with a variable optical attenuator (VOA) below the measured SBS threshold of the long span of single-mode fiber (SMF) that follows. The light then propagated the long length of SMF. The polarization of the light was then rotated with a polarization controller (PC) before impinging on the polarization beam splitter (PBS) so that

equal amounts of light emerged at each of the two outputs of the PBS. After exiting the outputs of the PBS, the light propagated along two length/phase matched paths, one of which contained a variable optical delay line (VODL) used to match its length to that of the other path. On each path, the light was sent to one of the two photodiodes comprising the balanced detector (photodiodes A & B), where each photodiode was biased with, and had its generated DC photocurrent measured by, a source meter.

Between the output of the CW laser and the outputs of the free-space polarization beam splitter (FSPBS) in Fig. 3.2, the light propagated as follows. Light sourced by the laser was launched along the slow axis of the attached PMF, passed through a PM isolator to severely attenuate any back reflected light from the Farady rotating mirror (FRM) propagating toward the laser, contacted the 45° PM splice, and was evenly distributed between the slow and fast principal polarization axes. The light then passed through a 50/50 PM optical coupler (50/50 PMOC), traversed a long span of SMF, and was retroreflected and had its fast and slow polarization axes rotated 90° by the FRM, which essentially flipped the fast and slow polarization axes. The reflected light then traveled back through the long span of SMF, through the 50/50 PMOC, and impinged on the FSPBS. The fast axis-polarized light was passed through the output of the FSPBS on the right and the light polarized along the slow axis was passed through the output of the FSPBS on the left.

Following the outputs of the FSPBS up through detection with the balanced detector, the following occurred with regard to the propagating light in Fig. 3.2. After leaving the two outputs of the FSPBS, the light propagated along two length/phase matched paths, one of which employed a VODL to match its length to that of the other path. On each path the light was sent through a 98/2 optical coupler (98/2 OC), with the majority of the light (approximately 98%) sent to one of the two photodiodes comprising the balanced detector (PDA & PDB) and the remaining small amount (approximately 2%) sent to an optical power meter (OPM) for measurement. The measured power of the light, coupling ratios of the optical couplers, and responsivities of the photodiodes were used to calculate the DC photocurrent sourced by each photodiode. See Appendix B for details.

The DC photocurrents were calculated using the aforementioned parameters, rather than biasing the photodiodes and measuring the DC photocurrents directly with source meters (SMA & SMB), as in the setup in Fig. 3.1, because the noise generated by the source meters was significantly high such that it obscured the measured noise due to DRS, even after low pass filtering the biases (see data plot in Fig. 3.3). Instead, low noise power supplies, with their outputs low pass filtered, were used to bias the balanced photodiodes. This reduced the noise generated by the power supplies to a level below that of the DRS noise (see data plot in Fig. C.3 of Appendix C).

The verbiage that follows refers to the reference frames shown in Figs. 3.1-3.2 and serves to describe the setups in more detail. The reference frames on the figures conceptually show the evolution of the polarized light at various points in the link along the propagation path. Pertaining to the experimental setup shown in each figure, the following occurred at each frame.

Fig. 3.1 reference frames:

- F1: All of the light emitted by the CW laser was transmitted along the slow axis of the PMF between the output of the laser and the input to the 45° PM splice.
- F2: The light at the output of the 45° PM splice was split evenly between the fast and slow axes, thus both the fast and slow axis polarization modes were populated. These modes are orthogonal to one another.
- F3: The fast axis-polarized light arrived prior to that polarized along the slow axis due to the strong birefringence (polarization-dependent index of refraction) of the PMF between the output of the 45° PM splice and the input of the VOA, which caused the fast and slow axis modes to separate spatially as they propagated. The intensities of both polarizations were attenuated by the VOA.
- F4: The fast and slow axis polarization modes arrived at the input of the PC with even more spatial separation between them, but still orthogonal to one another, and rotated relative to how they were oriented at the output of the VOA, due to the weak birefringence of the SMF. After being rotated by the PC, the slow axis-polarized light was oriented such that it impinged on the PBS so that equal amounts of the light were passed to each output of the PBS.
- F5: Half of the light input to the PBS was transmitted along the slow axis of the PMF coupled to the output of the beam splitter on the upper path.
- F6: The other half of the light input to the PBS was transmitted along the slow axis of the PMF coupled to the output of the beam splitter on the lower path.

Beyond reference frame 5, the polarization of the light does not matter for this application. However, along the two paths that follow frame 5, the relative RF phase of the noise/signal impressed on the light and the relative intensity of the light are important for the balanced detection process.

Fig. 3.2 reference frames:

- F1: All of the light emitted by the CW laser was transmitted along the slow axis of the PMF between the output of the laser and the input to the 45° PM splice.
- F2: The light at the output of the 45° PM splice was split evenly between the fast and slow axes, thus both the fast and slow axis polarization modes were populated. These modes are orthogonal to one another.
- F3: The fast axis-polarized light arrived prior to that polarized along the slow axis due to the strong birefringence of the PMF between the output of the 45° PM splice and the

input of the 50/50 PMOC (on top left of device), which caused the fast and slow axis modes to separate spatially as they propagated over the length L_1 .

- F4: The fast and slow axis polarization modes arrived at the FRM with even more spatial separation between them, but still orthogonal to one another, and rotated relative to how they were oriented at the output of the 50/50 PMOC, due to passing through the span of PMF (L_2), and the long length of SMF. In the FRM, the magnetic field induced by the magnets rotated the incoming light by 45° prior to the light contacting the mirror [1].
- F5: The light reflected off of the mirror, passed through the magnetic field of the FRM, and was rotated by another 45° before propagating back toward the 50/50 PMOC. Thus, the fast and slow axis polarizations leaving the FRM were rotated by 90° relative to how they were oriented when they entered the device [1].
- F6: The fast and slow axis polarization modes arrived at the input of the 50/50 PMOC (on bottom right of device) along the return path with approximately the same spatial separation between them as they had on the forward path, but with the fast and slow axis polarizations swapped.
- F7: The fast and slow axis polarization modes arrived at the input of the FSPBS with no spatial separation between them, just as they were when they left the output of the 45° PM splice in F2. The length of PMF on the return path, L_3 , was equal to that of L_1 on the forward path, and served to essentially compensate for the spatial separation between polarization modes along span L_1 .
- F8: The fast axis polarization mode input to the FSPBS was transmitted along the slow axis of the PMF coupled to the output of the beam splitter on the right path.
- F9: The slow axis polarization mode input to the FSPBS was transmitted along the slow axis of the PMF coupled to the output of the beam splitter on the left path.

After reference frame 7, the polarization of the light does not matter, but as mentioned previously, the relative RF phase of the noise/signal impressed on the light and the relative intensity of the light along the two paths that follow are important for balanced detection.

3.4 Results & Discussion

The single-sided output noise power spectral density of the links employing polarization multiplexing/de-multiplexing and balanced detection (Fig. 3.1) plus retroreflection (Fig. 3.2) was obtained by measuring RF power using an LNA and electrical spectrum analyzer (ESA) and normalizing to a 1 Hz bandwidth. The LNA was used to amplify the link noise above the noise floor of the ESA so that it could be measured. The output noise power spectral density values were then corrected for the gain and output noise of the LNA and cast in terms of optical RIN. Plots of the obtained optical RIN spectrum for each link are shown in Figs. 3.3-3.4. Additional plots showing the output noise power spectral density of the entire link, that is the optical section plus the RF section, and the output noise power spectral density of the optical section are

provided in Appendix C. Equations used to calculate output noise power spectral density and RIN (pp. 60-70 in [2]) are also contained in Appendix C.

By examining Fig. 3.3 it can be seen that the polarization multiplexing/de-multiplexing scheme using balanced detection (red trace) reduced noise relative to that using just a single photodiode (green trace). The amount of noise reduction for balanced detection (photodiodes A & B) versus detection with one photodiode (photodiode A) was measured to be ~2 to 8 dB from 25 kHz to 1.5 MHz and ~1 to 5 dB from 3.5 to 5 MHz for DC photocurrents of 1.0 mA (photodiode A) and -1.0 mA (photodiode B). The high noise levels measured from 10 to 25 kHz and 1.5 to 3.5 MHz are due to noise from the source meters (power supplies) used to bias the photodiodes and measure their generated DC photocurrents. Power supply noise is shown by the orange trace. Also shown is the measured noise floor of the ESA (black trace); the calculated shot noise limit for 1.0 and -1.0 mA of photocurrent, 2 mA total (purple trace); and the calculated level due to superposed shot and LNA noise (gray trace).

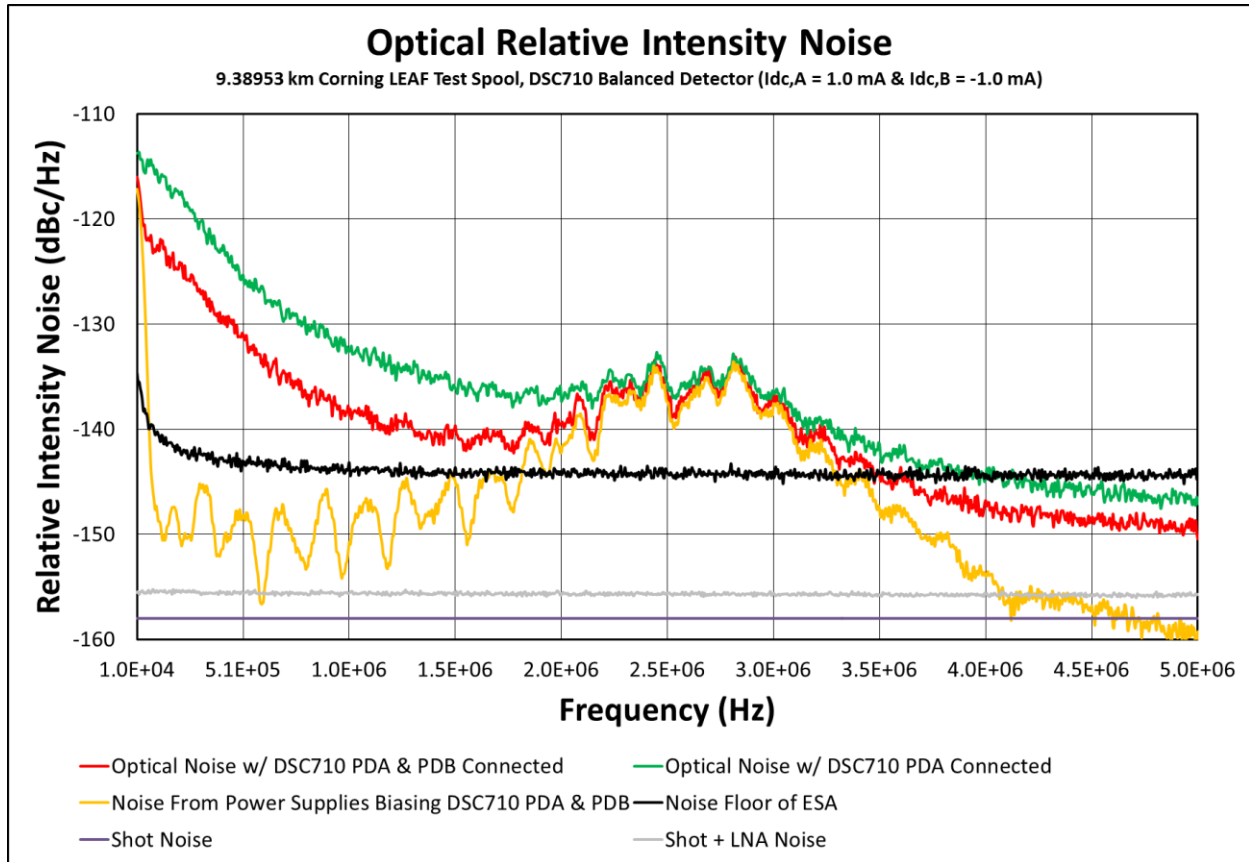


Fig. 3.3: Optical RIN spectrum for link utilizing polarization multiplexing/de-multiplexing and balanced detection to reduce noise due to DRS.

As can be seen by viewing Fig. 3.4, the polarization multiplexing/de-multiplexing scheme using balanced detection and retroreflection (blue trace) did not reduce noise relative to that using a

single photodiode (red trace). The measured noise level for balanced detection (photodiodes A & B) compared to that for detection with one photodiode (photodiode A) was ~3 to 5 dB higher between 10 kHz and 3 MHz at DC photocurrents of 0.070 mA (photodiode A) and -0.070 mA (photodiode B). The low DC photocurrents for this link (Fig. 3.2) relative to those for the link in Fig. 3.1 resulted from the optical loss associated with the double pass through the 50/50 optical coupler and long span of SMF, as well as the loss through the FRM and FSPBS.

As another check to see whether cancellation of a coherent RF signal could be obtained using the link employing polarization multiplexing/de-multiplexing, balanced detection, and retroreflection, a 200 kHz RF tone was input to the link via a quadrature biased single-input/single-output Mach-Zehnder modulator (MZM), which was placed between the laser and PM isolator in Fig. 3.2. As expected, and shown in Fig. 3.4, the amplitude of the RF tone was greatly reduced after detection with the balanced detector, photodiodes A & B, (orange trace) compared to after it was detected with a single photodiode, photodiode A (green trace). The difference in amplitude between the RF tone measured after detection with photodiode A and that measured after detection with photodiodes A & B was ~17 dB. For the amplitude of the RF tone to have been increased rather than reduced a different link architecture would be needed, such as a link employing a dual-output MZM with a 180° relative RF phase between the two outputs, two separate spans of RF-phase-matched fiber, and a balanced detector (pp. 215-216 in [2]). As was demonstrated, the link employing polarization multiplexing/de-multiplexing, balanced detection, and retroreflection cancels a coherent RF signal but does not cancel noise.

The other traces shown on Fig. 3.4 are the measured noise floor of the ESA (black); the calculated shot noise for 0.070 and -0.070 mA of photocurrent, 0.140 mA total (purple); and the calculated shot plus LNA noise (gray).

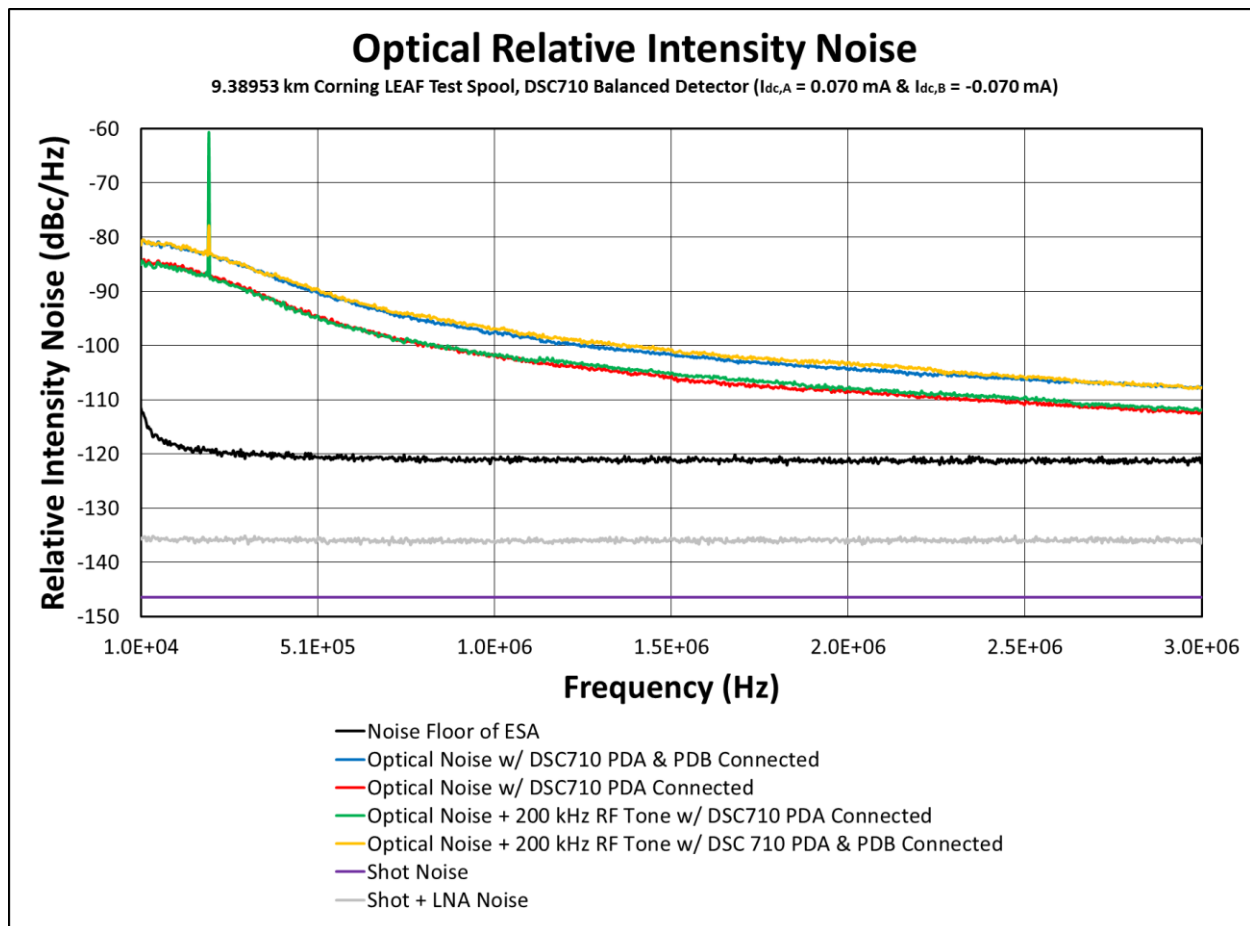


Fig. 3.4: Optical RIN spectrum for link utilizing polarization multiplexing/de-multiplexing, balanced detection, and retroreflection to address noise due to DRS.

3.5 Conclusions & Recommendations

The link employing polarization multiplexing/de-multiplexing and balanced detection (Fig. 3.1) was effective at reducing low-frequency noise in the RF domain due DRS-induced RIN in the optical domain, whereas the link utilizing the aforementioned plus retroreflection (Fig. 3.2) was not.

Further investigation is needed to determine whether RIN due to DRS is polarization dependent.

Recommend revising noise reduction techniques and further investigating whether RIN caused by DRS is polarization dependent.

4 Experiment 2: Techniques to Reduce Phase Noise in the RF Domain

Two sets of phase noise tests were conducted: absolute phase noise and residual phase noise tests.

The absolute phase noise tests entailed driving the device under test (DUT) with a state-of-the art low-phase noise RF oscillator and measuring the single-sideband (SSB) phase noise of the DUT against another low-phase noise RF oscillator of the same make and model that served as the reference for the measurement [3]. The DUTs for this set of measurements were two photonic links and an RF component in the link. The phase noise of the oscillator used to stimulate the DUTs was also measured against the reference and compared to that of the DUTs.

The residual phase noise tests involved stimulating the DUT with a state-of-the art low-phase noise RF oscillator and measuring the SSB phase noise of the DUT against that of the oscillator driving the DUT, with the oscillator serving as the reference [3]. The DUTs for this set of tests were five variants of a photonic link. Link architecture, component biases, and DC photocurrent levels were varied in a controlled fashion during the tests to assess their impact on measured close-in RF phase noise.

4.1 Purpose

This experiment was conducted to:

- Optimize link architecture, component biases, and DC photocurrent level to minimize close-in RF phase noise.

4.2 Objectives

The goals of this experiment were to determine the following:

- Optimal photodiode and low-phase noise amplifier bias voltages to minimize close-in RF phase noise.
- Optimal level of DC photocurrent to minimize close-in RF phase noise.
- Impact of fiber length on close-in RF phase noise.
- Impact of DCM on close-in RF phase noise.

4.3 Experimental Setup

Diagrams showing the absolute and residual phase noise measurement setups utilized for this experiment are shown in Fig. 4.1-4.2. The instrumentation and components shown in the figures are listed in Tables A.2 and A.5 in Appendix A.

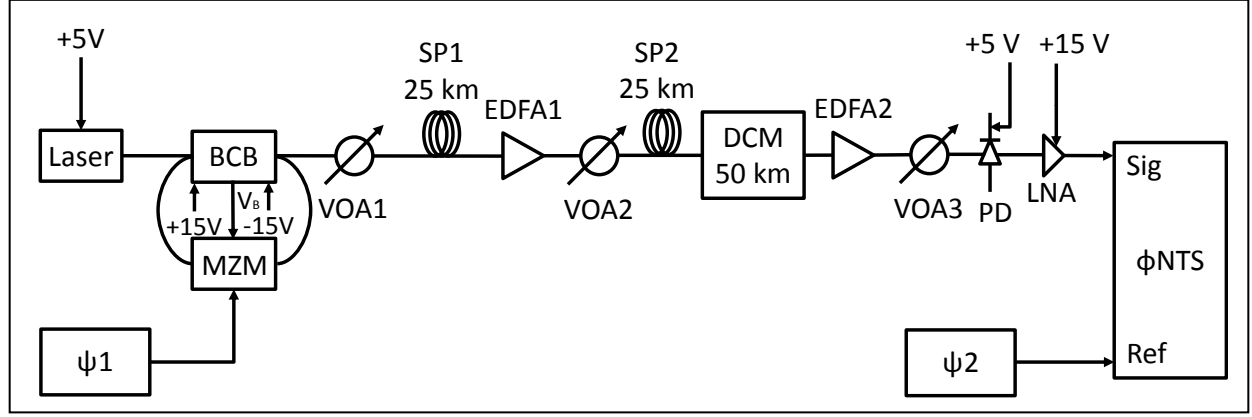


Fig. 4.1: Absolute phase noise measurement setup.

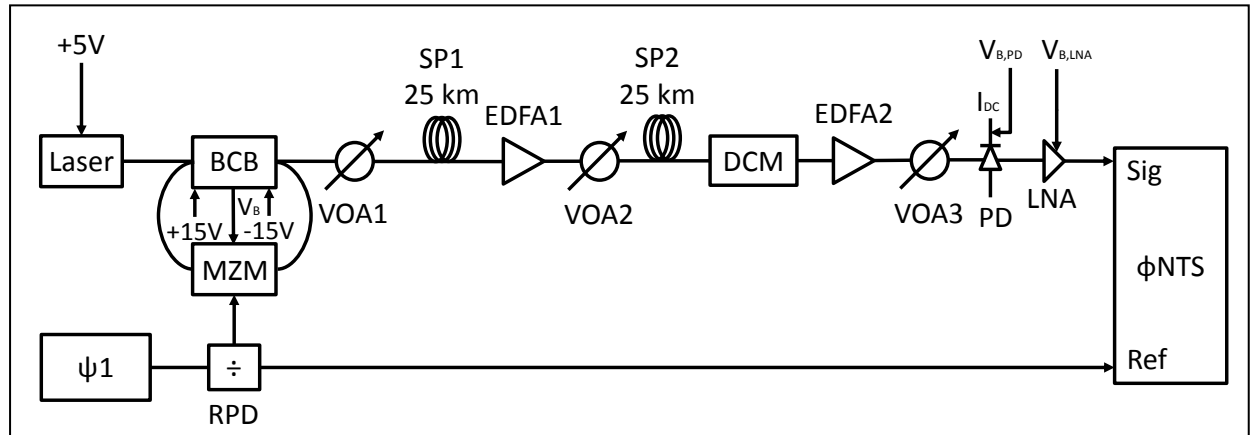


Fig. 4.2: Residual phase noise measurement setup. $V_{B,PD}$: photodiode bias voltage, I_{DC} : DC photocurrent, and $V_{B,LNA}$: low-phase noise amplifier bias voltage.

A description of the setup in Fig. 4.1 is as follows. Light sourced by a CW laser was input to a bias control board (BCB) that was used to set and hold the bias of the MZM at a quadrature point, modulated via an MZM driven by a 10.24 GHz RF oscillator, ψ_1 , and sent back through the BCB. The modulated light then went through the rest of the link, containing VOAs, spools of SMF, erbium doped fiber amplifiers (EDFAs), and a DCM prior to detection and demodulation back to RF with a photodiode. The RF output of the photodiode was then amplified with a low-phase noise amplifier to a measurable level, input to the signal port of the phase noise test set, phase detected, and compared against the detected phase of the 10.24 GHz RF oscillator connected to the reference port, ψ_2 , to yield the RF phase noise of the link [4]. The

VOAs were used to keep the optical power below the SBS threshold of the 25 km lengths of fiber, and the EDFAs were used to compensate for the loss through the two 25 km fiber spools (SP1 & SP2) and the DCM. The DCM was used to compensate for the chromatic dispersion of the two 25 km fiber spools.

The setup in Fig. 4.2 is similar to that in Fig. 4.1 described above, except for the following two differences. The VOAs and EDFAs in the Fig. 4.2 setup were not just used to compensate for the loss through the fiber spools and the DCM, but were also used to set the optical power incident on the photodiode to a level necessary to achieve the desired DC photocurrent. The output of the 10.24 GHz RF oscillator, ψ_1 , was split with a 50/50 RF power divider; one half was used to stimulate the link and the other half was used as the reference. As mentioned above, the RF output of the link was phase detected and compared against the phase of the reference to yield the RF phase noise of the link. However, in this case the reference was the same 10.24 GHz RF oscillator used to stimulate the link, ψ_1 , rather than a separate 10.24 GHz RF reference oscillator, ψ_2 .

4.4 Results & Discussion

Four absolute phase noise tests were conducted using the apparatus shown in Fig. 4.1. Test 1 entailed measuring the phase noise of the entire link shown in the figure. Test 2 involved measuring the phase noise through the shown link, less the two 25 km spools of SMF, both EDFAs, the 50 km DCM, and VOAs 2 & 3. The phase noise of just the low-phase noise amplifier (low phase-noise LNA) and ψ_1 were measured during tests 3 and 4, respectively.

A plot of the absolute SSB phase noise measured during the four tests is shown in Fig. 4.3. By viewing the plot it can be seen that the level of the phase noise measured during the four tests is approximately the same out to about 28 Hz, where the phase noise measured during test 1 starts to increase relative to that measured during the other tests and remains higher out to 10 MHz. The phase noise measured during test 2 tracks that measured during tests 3 and 4 out to approximately 1 kHz, where it starts to grow compared to that measured during the other tests and remains higher over the remainder of the measurement band. The phase noise measured during test 3 is approximately equal to that measured during test 4 out to about 3.7 kHz, where it starts to exceed that measured during test 4 and continues to do so across the rest of the frequency range of the measurement.

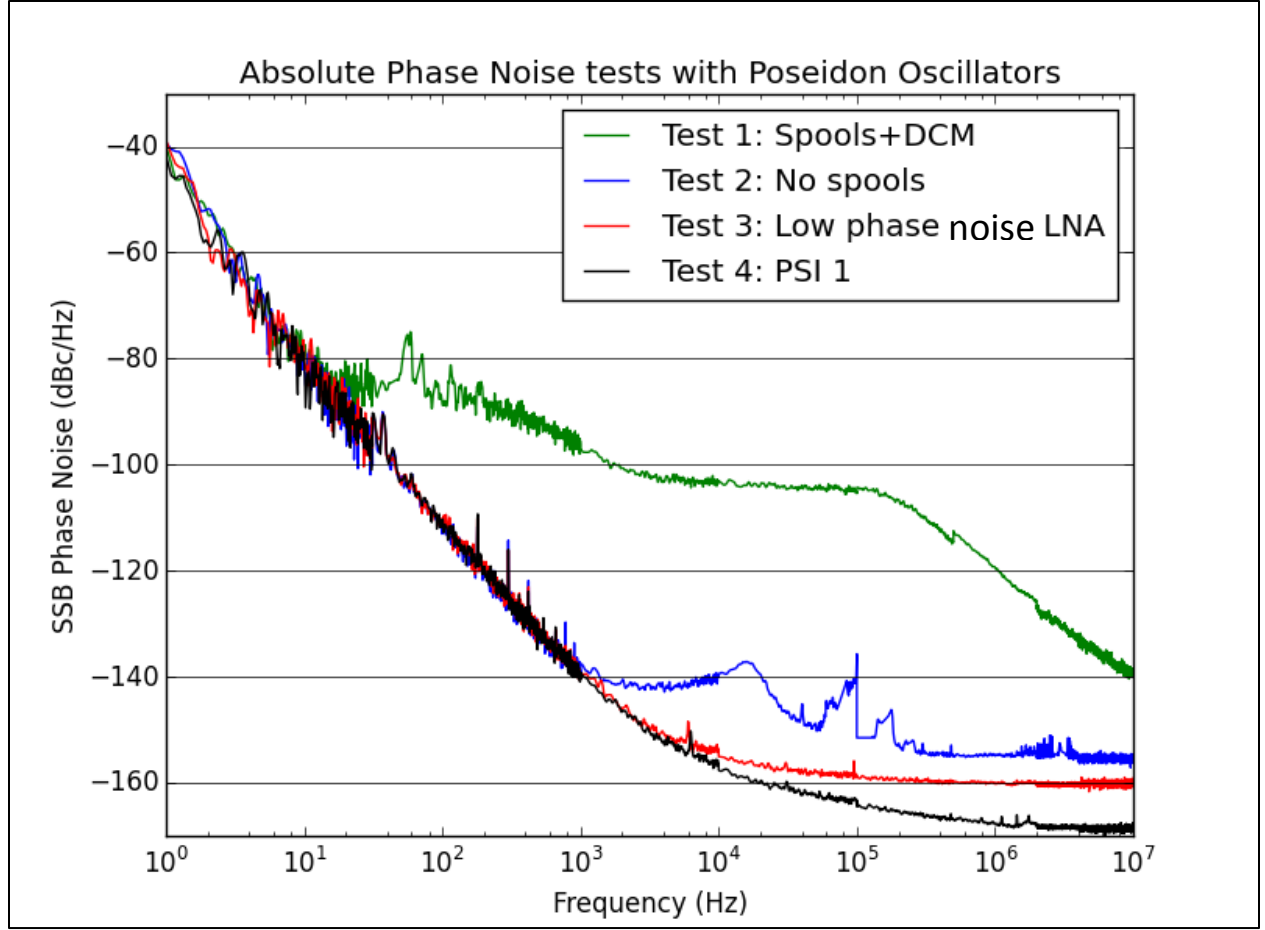


Fig. 4.3: Measured SSB phase noise spectra for the four absolute phase noise tests. The frequency axis shows the frequency offset from 10.24 GHz.

Eight residual phase noise tests were performed using five variants of the link shown in Fig. 4.2. A description of the tested variants is provided in Table 4.1. The conducted tests along with the associated variants, photodiode bias voltages, DC photocurrents, and low-phase noise amplifier bias voltages are noted in the test matrix shown in Table 4.2.

Table 4.1: Variants of the link evaluated during the residual phase noise tests.

Variant	Description
1	Link in Fig. 4.2 w/ 50 km DCM and DSC30S photodiode
2	Link in Fig. 4.2 w/ 20 km DCM & DSC30S photodiode, less EDFA1, VOA2, & SP2
3	Link in Fig. 4.2 w/ DSC30S photodiode, less DCM
4	Link in Fig. 4.2 w/ DSC50S photodiode, less DCM
5	Link in Fig. 4.2 w/ DSC50S photodiode, less DCM, EDFA1, VOA2, & SP2

Table 4.2: Test matrix showing executed residual phase noise tests.

Test	Variant	Photodiode Bias Voltage (V)	DC Photocurrent (mA)	Low-Phase Noise Amplifier Bias Voltage (V)
1	1	5	5	12
2	2	5	5	12
3	3	5	5	12
4	3	5	5	15
5	4	5	10	15
6	4	5	15	15
7	5	5	15	15
8	5	4	20	15

A plot of the residual SSB phase noise measured during the tests conducted with two 25 km spools of SMF is shown in Fig. 4.4. By viewing the figure it can be seen that the level of the phase noise measured during the tests is approximately the same out to about 5 Hz, where the phase noise measured during tests 1 and 3 exceeds that measured during the other tests out to about 1 MHz and 10 kHz, respectively. The phase noise measured during test 1 is higher than that measured during test 3 between approximately 300 Hz and 1 MHz, whereas that measured during test 3 is higher than that measured during test 1 from about 5 Hz to 30 Hz. The phase noise levels measured during tests 4, 5, and 6 are very similar over the entire frequency range of the measurement.

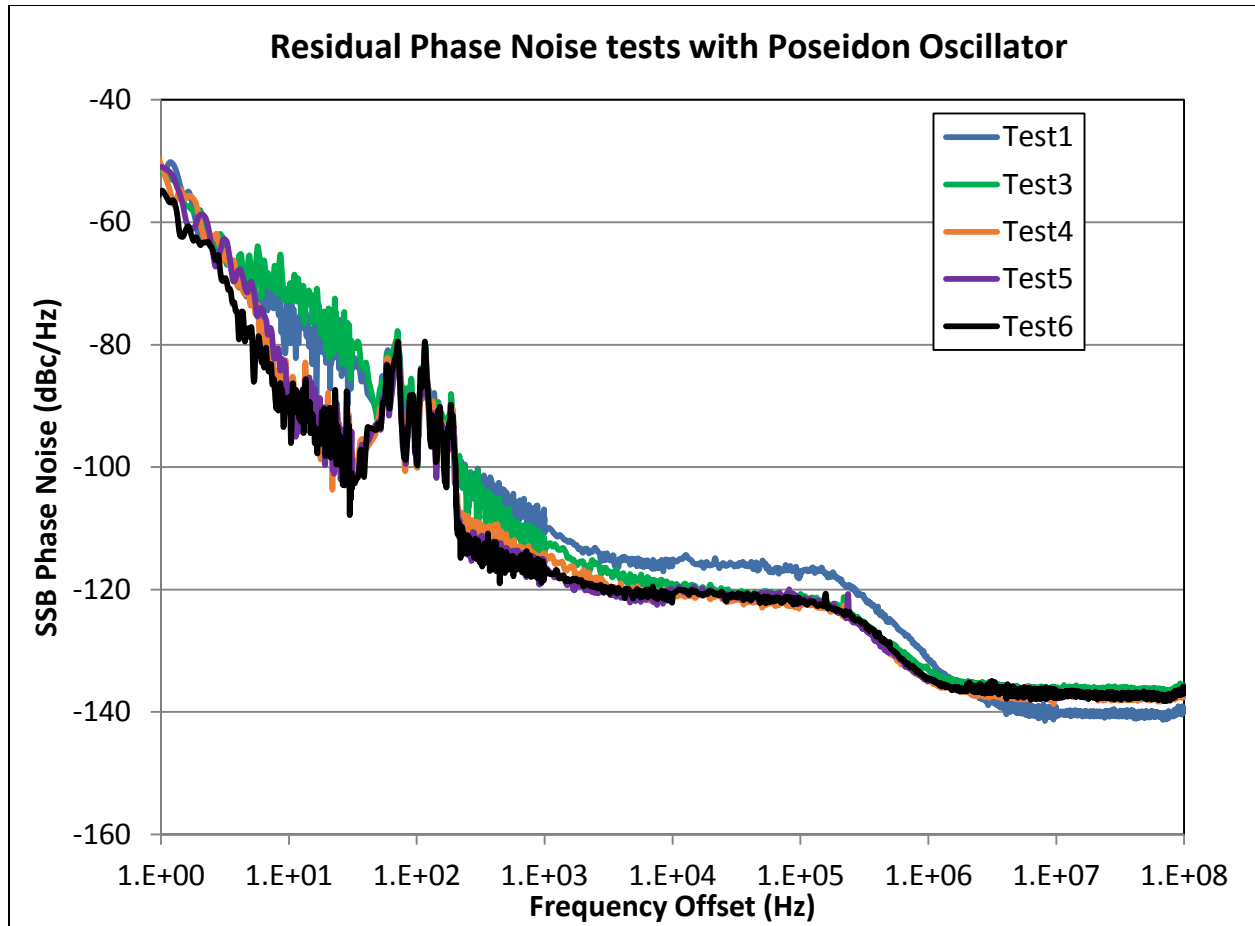


Fig. 4.4: Measured SSB phase noise spectra for the residual phase noise tests conducted with two 25 km spools of SMF. The frequency offset is from 10.24 GHz.

The residual SSB phase noise measured during the tests performed with one 25 km spool of SMF is shown on the plot in Fig. 4.5. By examining the figure it can be seen that the phase noise measured during test 2 is higher than that measured during tests 7 and 8 from 1 Hz to approximately 3 MHz. Of note are prominent features in the test 2 data near 3.5 kHz and 7 kHz, as well as between 10 kHz and 100 kHz. The phase noise levels measured during tests 7 and 8 are approximately the same across the entire bandwidth of the measurement, except from about 1 kHz to 100 kHz where there are features in the test 8 data set which are not present in the test 7 data.

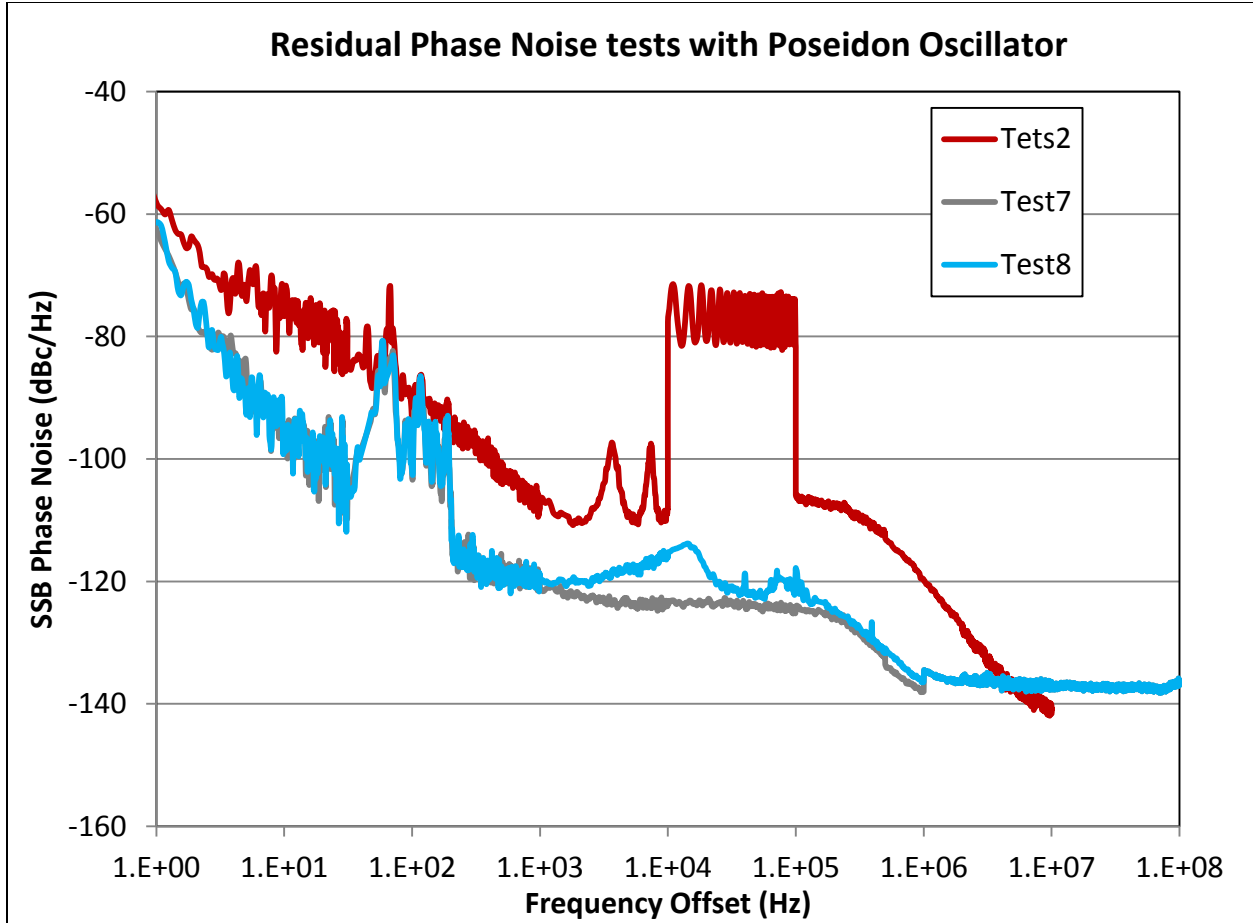


Fig. 4.5: Measured SSB phase noise spectra for the residual phase noise tests conducted with one 25 km spool of SMF. The frequency offset is from 10.24 GHz.

A comparison of the SSB phase noise measured during all eight of the residual phase noise tests is shown in Fig. 4.6. It can be seen by inspecting the figure that there is a feature in the measured data from approximately 30 Hz to 200 Hz, which is common across all of the tests. Also of note is that the phase noise measured during test 7 is lower than that measured during the other tests over the entire frequency range of the measurement. The link utilized for test 7 contained one 25 km spool of SMF; no DCM; an EDFA plus two VOAs, one on either side of the spool, for optical amplitude control; and a low-phase noise amplifier to boost the RF output of the DSC50S photodiode. For this combination, the applied photodiode and low-phase noise amplifier bias voltages were 5 V and 15 V, respectively, and the DC photocurrent sourced by the photodiode was 15 mA.

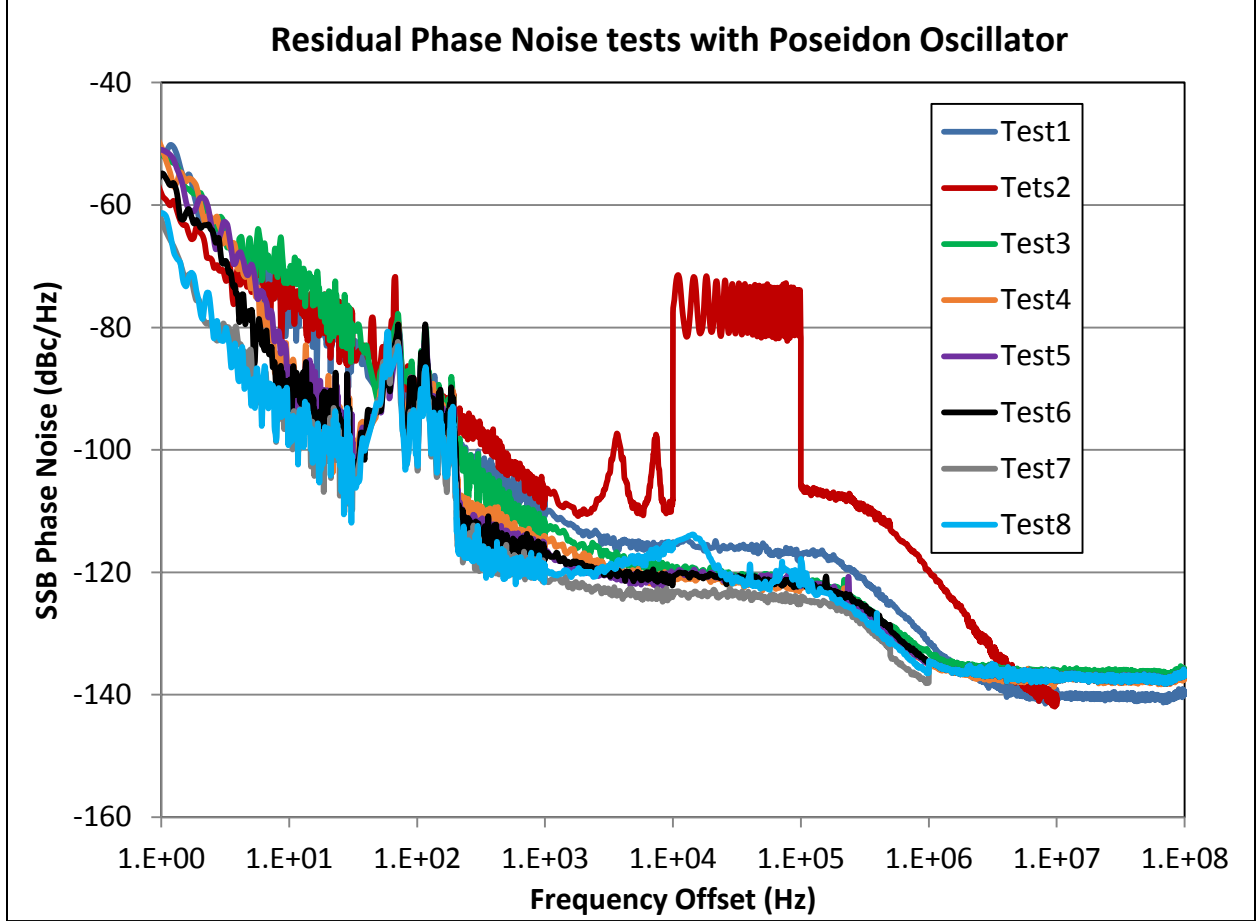


Fig. 4.6: Comparison of measured SSB phase noise from all eight residual phase noise tests. The frequency offset is from 10.24 GHz.

4.5 Conclusions & Recommendations

Operating the low-phase noise amplifier at the highest allowable voltage (15 V) minimized close-in RF phase noise.

Operating the photodiode at high voltage (5 V) and moderate DC photocurrent (15 mA) reduced close-in RF phase noise. Increasing DC photocurrent did not significantly affect close-in phase noise; however, decreasing photodiode bias voltage to 4 V caused an increase in phase noise in certain areas (between 1 kHz and 100 kHz).

Using a shorter length of single-mode fiber in the link and no DCM yielded a reduction in close-in RF phase noise.

To minimize close-in RF phase noise, recommend constructing a link that includes a low-phase noise amplifier and as short a fiber span as practical for the application, operating the photodiode and low-phase noise amplifier at their highest allowable voltages, and operating the link at an optical power level that produces moderate DC photocurrent.

5 Experiment 3: Fiber-Based Optoelectronic Oscillators

Three fiber-based OEO structures were built and tested: a generic OEO, an OEO employing retroreflection, and an OEO with a proposed RF phase noise cancellation scheme.

The generic OEO consisted of a basic photonic link that had its RF output conditioned and injected into the RF input of the MZM at the front-end of the link, such that self-sustained oscillation occurred in the RF domain.

The OEO with retroreflection was similar to the generic OEO; except that retroreflection was used to effectively double the length of the fiber span in the link to improve the quality factor/reduce the RF phase noise of the OEO.

The third structure consisted of two parts: one was a generic OEO and the other was a basic photonic link employing similar optical and RF hardware as the OEO, both of which shared the same span of SMF. The key differences between the two were that each had its own CW laser source, with the lasers operating at different wavelengths, and that the MZM in the photonic link was driven with a low-phase noise RF source rather than with its own RF output as in the OEO.

If the measured RF phase noise of the OEO, operating on one laser wavelength, and the photonic link, operating on another, is similar, then the assumption is that the phase noise of the photonic link, which is also common to the OEO since the two share the same span of SMF, could be used to reduce the overall phase noise of the OEO. This reduction in phase noise could be realized by measuring the phase noise of the OEO relative to that of the photonic link and subtracting the phase noise of the photonic link from that of the OEO.

5.1 Purpose

This experiment was conducted to:

- Determine feasibility of close-in RF phase noise cancellation with the proposed scheme.

5.2 Objectives

The goals of this experiment were the following:

- Measure close-in RF phase noise of OEO with proposed RF phase noise cancellation scheme:
 - Phase noise of OEO
 - Phase noise of photonic link
 - Phase noise of OEO versus phase noise of photonic link
- To determine whether RF phase noise imposed on one laser wavelength could be used to cancel that impressed on another laser wavelength to reduce the overall close-in phase noise in the RF domain.

5.3 Experimental Setup

Diagrams of the three OEO structures are shown in Figs. 5.1-5.3. The instrumentation and components shown in the figures are listed in Tables A.3 and A.6 in Appendix A.

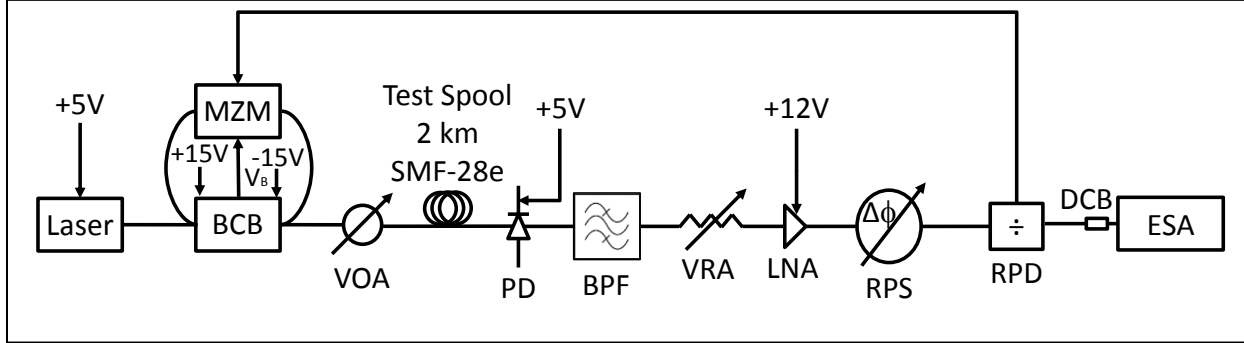


Fig. 5.1: Generic OEO with a 2 km span of SMF. The optical power input to the photodiode was 9.08 dBm, the DC photocurrent was 5.84 mA, and the RF power input to the MZM was 6.02 dBm, where the small-signal RF gains of the optical and RF sections were -20.55 dB and 20.33 dB, respectively.

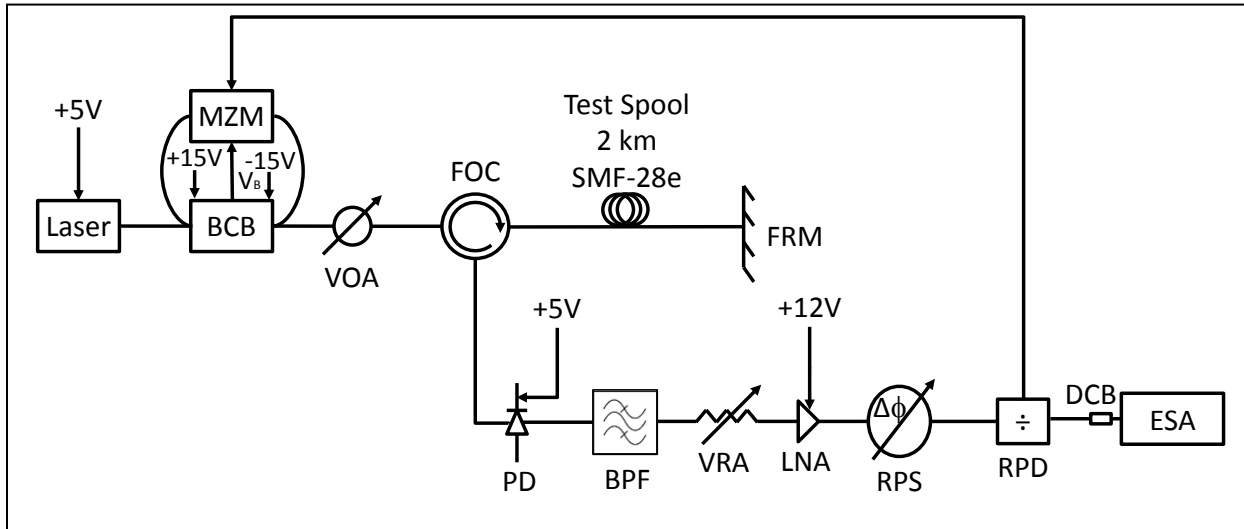


Fig. 5.2: OEO utilizing a FRM to produce retroreflection, which effectively doubles the length of the 2 km span of SMF shown. The optical power input to the photodiode was 6.88 dBm, the DC photocurrent was 3.68 mA, and the RF power input to the MZM was 7.01 dBm, where the small-signal RF gains of the optical and RF sections were -25.56 dB and 25.55 dB, respectively.

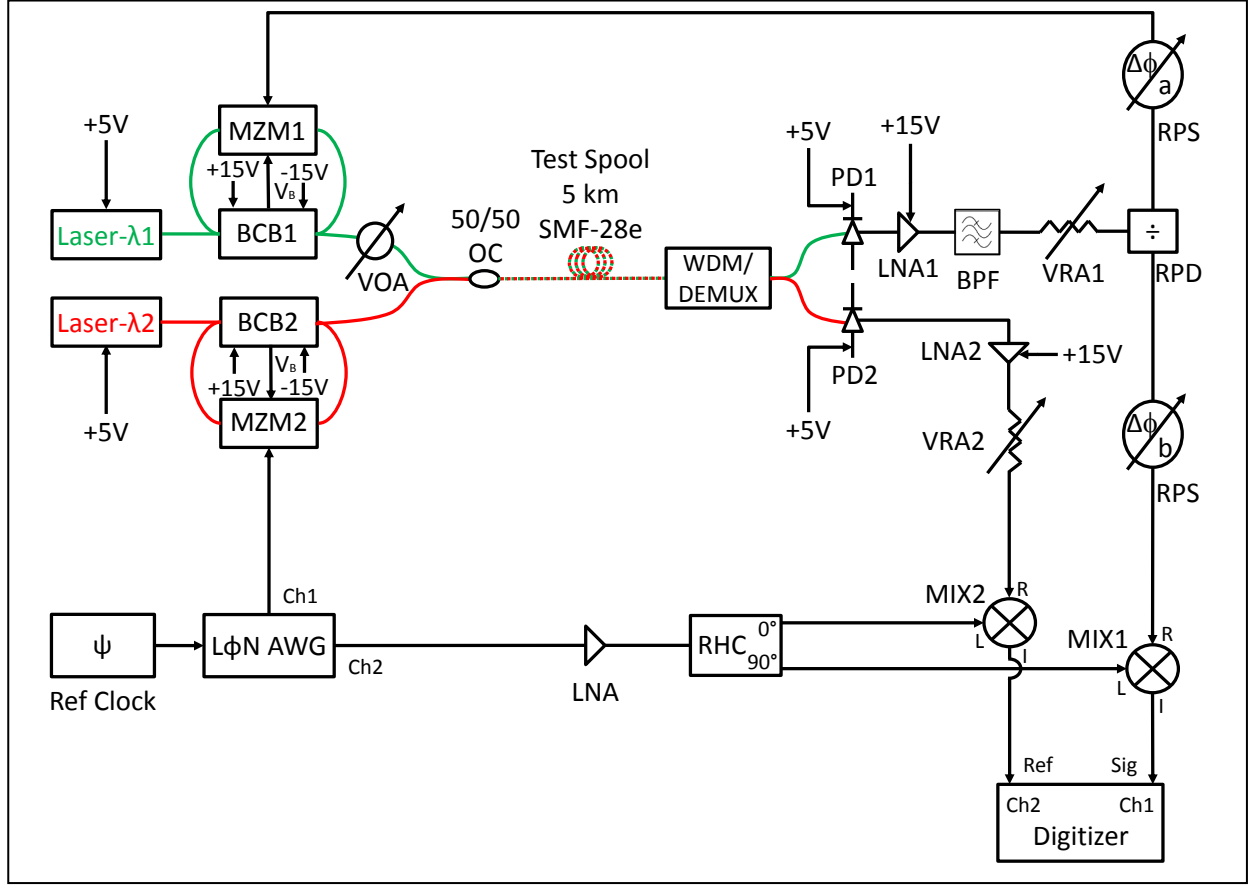


Fig. 5.3: OEO with proposed RF phase noise cancellation scheme. The optical power levels input to the photodiodes in the OEO (green) and photonic link (red) were 4.55 dBm and 3.83 dBm, respectively; the DC photocurrents in the OEO and photonic link were 2.32 mA and 1.90 mA, respectively; and the RF power input to both MZMs was 7.03 dBm. The small-signal RF gains of the optical and RF sections of the OEO were -27.50 dB and 27.16 dB, respectively, and those for the photonic link were -34.57 dB and 34.28 dB, respectively. λ_1 : laser wavelength of OEO (1550.12 nm) and λ_2 : laser wavelength of photonic link (1553.33 nm).

The following is a description of the setup in Fig. 5.1. Light emitted by a CW laser was input to a BCB used to set and hold the MZM bias at quadrature, modulated with an MZM driven by the RF output of the OEO (10.24 GHz), and sent back through the BCB. From here, the modulated optical signal was attenuated with a VOA below the SBS threshold of the 2 km span of SMF. The RF-modulated light then propagated the 2 km length of SMF and was detected and down converted back to RF with a photodiode. The RF signal output by the photodiode was then band pass filtered, attenuated with a variable RF attenuator (VRA), amplified with an LNA, passed through an RF phase shifter (RPS), and split with a 50/50 RF power divider. Half of the RF signal was sent to an ESA for measurement and the other half was input to the MZM to drive the OEO. The VRA was used to attenuate the RF signal below the 1-dB compression point of the

LNA, and was also used in combination with the VOA and LNA to appropriately set the RF gain of the OEO such that self-sustained oscillation occurred.

When the net RF gain of the loop comprising the OEO, that is the RF gain of the optical section plus the RF section, was just under unity one of the OEO cavity modes would resonate. Cavity modes near the center frequency of the filter within the pass band were fed into the RF input of the MZM. The mode with slightly higher amplitude than the others on the initial pass through the cavity experienced a large increase in amplitude relative to the other modes after many subsequent passes, given adequate RF gain of the loop, and became the dominant or fundamental mode driving the OEO. The amplitude of the modes was dictated by noise generated by the active components in the loop, which served to seed the OEO, and the net RF gain of the loop. Since the amplitude of the noise fluctuated randomly the amplitude of the modes also fluctuated randomly during seeding, so each time the active components in the OEO were energized, the OEO would not consistently resonate at the same frequency. Also, the cavity length of the OEO changed slowly with temperature, so the frequency of the fundamental and side modes drifted as a function of temperature. The RF phase shifter was used to tune the frequency of the fundamental mode to compensate for the drift.

The setup in Fig. 5.2 is identical to that in Fig. 5.1, with the exception of a fiber-optic circulator (FOC) and FRM. The FOC served to route the light modulated at 10.24 GHz toward the FRM on the forward path and the retroreflected light on the return path toward the photodiode, while isolating the light on the return path from the laser. The role of the remaining components in the loop and generation of the fundamental mode are the same as discussed above for the structure in Fig. 5.1.

The structure shown in Fig. 5.3 is comprised of a generic OEO, similar to that shown in Fig. 5.1 and described in the above paragraphs, and a basic photonic link. The upper portion of Fig. 5.3 including the green path (optical) from Laser- λ_1 and the black path (RF) to the input of MZM1 is the OEO, and the lower portion of the figure including the red path (optical) from Laser- λ_2 and the black path (RF) to the channel 2 input of the digitizer is the photonic link.

Modulated light on the OEO and photonic link paths, modulated at the same RF drive frequency (2.40 GHz), was wavelength division multiplexed with a 50/50 optical coupler, passed through a 5 km span of SMF, wavelength division de-multiplexed with a WDM/DEMUX, and passed to separate photodiodes, PD1 and PD2. The RF output of PD1 was amplified, filtered, attenuated, and split with a 50/50 RF power divider. Half the power was input to MZM1 and used to drive the OEO. The other half was input to the RF port of mixer 1. The RF output power of PD2 was adjusted with an LNA and VRA, so that the power input to the RF port of mixer 2 was approximately equal to that input to the OEO and the RF port of mixer 1. The RF phase shifter, $\Delta\phi_a$, in the OEO was used to tune the frequency of the fundamental mode, and that on the path from PD1 to the RF input of mixer 1, $\Delta\phi_b$, was used to tune the relative RF phase between this

path and the path from PD2 to the RF input of mixer 2. The net RF gain of the OEO was controlled with the VOA and VRA1.

The 2.40 GHz RF signal input to the RF ports of mixers 1 and 2 on the OEO and photonic link paths, respectively, was mixed with a 2.4007323 GHz local oscillator signal to produce a 732.3 kHz difference frequency used for the phase noise measurement. The local oscillator signal, as well as the RF drive for the photonic link, was provided by a low-phase noise arbitrary waveform generator, L ϕ N AWG, utilizing a 10.24 GHz state-of-the-art RF oscillator, ψ , as its low-phase noise external reference clock. The local oscillator signal was amplified and fed into a quadrature hybrid RF coupler, RHC, which output in-phase and quadrature components of the local oscillator that were fed into mixers 2 and 1, respectively. The output of mixer 1 was the difference in frequency between the local oscillator and the OEO drive frequency, whereas the output of mixer 2 was the frequency difference between the local oscillator and the photonic link drive frequency. The outputs of mixers 1 and 2 were input to channels 1 and 2 of the digitizer, respectively, and digitized at 10 MSa/s. From the digitized time-domain data, the phase noise was determined to be proportional to the phase difference between the RF outputs of the OEO and photonic link. The time-domain data were Fourier transformed to the frequency-domain and expressed as RF phase noise as a function of frequency offset from the 2.40 GHz RF drive.

5.4 Results & Discussion

Six measurements were taken on the three OEO structures: mode spacing, net RF gain of loop that yielded fundamental mode, fundamental-to-first-order side mode ratio, frequency drift, DC photocurrent fluctuation, and SSB phase noise, with the latter being of utmost importance. The first two measurements were taken on all three structures, the third on the structures in Figs. 5.1 and 5.3, and the remaining three on the structure in Fig. 5.3. The measured values are shown below in Table 5.1.

Three SSB phase noise measurements were taken on the structure in Fig. 5.3: the baseline phase noise of just the OEO, the baseline phase noise of just the photonic link, and the phase noise of the OEO compared to that of the photonic link. The baseline measurements were taken against the low-phase noise arbitrary waveform generator, which served as the reference, whereas for the comparison, the phase noise of the OEO was measured against the photonic link, which was used as the reference. The exact same measurement setup described above in reference to Fig. 5.3 was used for the measurement of OEO versus photonic link phase noise.

A modification to the setup in Fig. 5.3 was used for the baseline measurements of the OEO and photonic link phase noise. For the OEO baseline measurement, the RF output from channel 1 of the low-phase noise arbitrary waveform generator was disconnected from MZM2 and injected into the RF input of mixer 2, the RF output of the photonic link was terminated in a 50 Ω load, and the RF output of the OEO was fed into the RF input of mixer 1. Similarly, for the photonic link baseline phase noise measurement, the RF output from channel 1 of the low-phase noise

arbitrary waveform generator was split, half was used to drive MZM2 and the other half was sent to the RF input of mixer 2; the RF output of the OEO was disconnected from mixer 1 and terminated in a $50\ \Omega$ load; and the RF output of the photonic link was injected into the RF input of mixer 1. The outputs of the mixers, providing the difference frequencies for the measurements, were input to channels 1 and 2 of the digitizer, respectively.

Table 5.1: Results of measurements taken on the three OEO structures.

		<i>OEO Structure</i>		
		Generic OEO (Fig. 5.1)	OEO w/ retroreflection (Fig 5.2)	OEO w/ RF phase noise cancellation (Fig 5.3)
<i>Measurement</i>	Mode spacing (kHz)	101	50.5	40.4
	Net RF gain of loop that yielded fundamental mode (dB)	-0.17	-0.01	-0.34
	Fundamental-to-first-order side mode ratio (dB)	56	Not measured	50
	Frequency drift (Hz/min)	Not measured	Not measured	250
	DC photocurrent fluctuation (mA)	Not measured	Not measured	± 0.05
	SSB phase noise (dBc/Hz)	Not measured	Not measured	See Fig. 5.4

A plot of the measured SSB phase noise of the OEO with RF phase noise cancellation (Fig. 5.3) is shown in Fig. 5.4. The red trace is the phase noise of the OEO (OEO baseline data) and the blue trace is the phase noise of the photonic link (fiber baseline data). It can be seen by viewing the figure that the phase noise of the OEO is greater than that of the photonic link out to about 10 kHz, with the difference in average phase noise between the two decreasing with increasing frequency offset: ~ 33 dB at 1 Hz, ~ 28 dB at 10 Hz, ~ 25 dB at 100 Hz, ~ 9 dB at 1 kHz, and ~ 3 dB at 10 kHz. Beyond 10 kHz, the phase noise levels flatten out over the remainder of the measurement bandwidth out to 1 MHz, with the exception of the OEO side modes and spurs in the photonic link spectrum. The first-order OEO side mode is at 40.4 kHz and the higher-order side modes are at integer multiples of the first-order side mode, where the mode spacing is set by the length of the OEO cavity (5 km fiber span plus additional short lengths of fiber pig tails and RF cables).

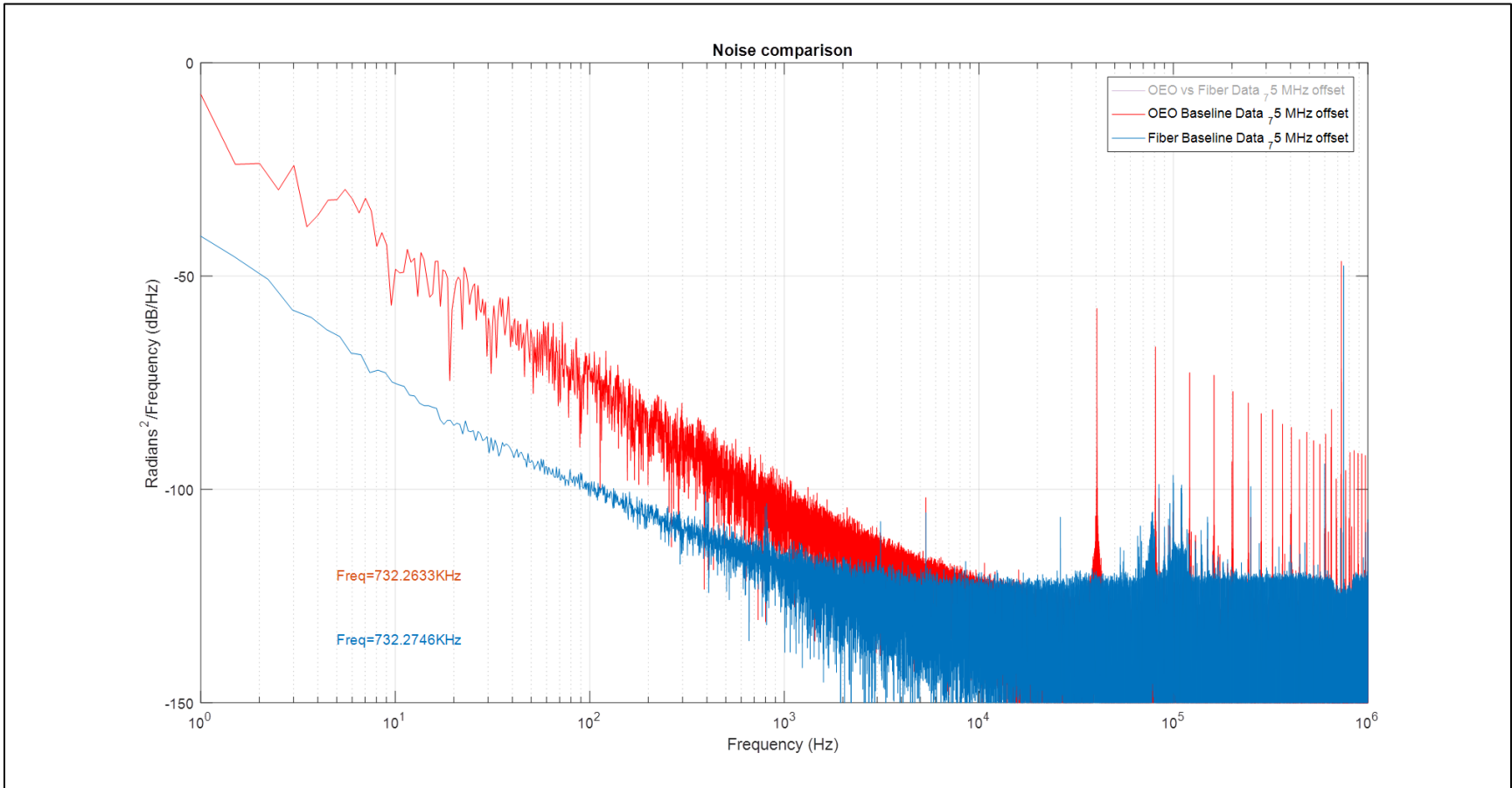


Fig. 5.4: Measured SSB phase noise spectra of OEO with RF phase noise cancellation. The red trace is the OEO phase noise (OEO baseline data) and the blue trace is the phase noise of the photonic link (fiber baseline data). The 732.3 kHz frequency displayed on the figure and shown as a large peak (~ -47 dBc/Hz) in the OEO and photonic link spectra is a beat tone that was used for the measurement. The frequency axis shows the frequency offset from 2.40 GHz.

The phase noise of the OEO is higher than that of the photonic link for two main reasons. The first reason is that the photonic link was driven with a lower phase noise source than the OEO, which was driven with its fundamental mode. Secondly, the phase noise in the OEO was accumulated over many trips through the cavity rather than over a single pass as in the photonic link, due to the architectural differences of the two paths. The phase noise in the OEO from a previous pass added with that of current and future passes, indicating that the OEO is a system with memory unlike the photonic link.

Reliable data showing RF phase noise cancellation was not obtained due to components in the measurement setup being out of specification: a 50/50 RF power divider and a quadrature hybrid RF coupler. These components yielded a relative RF phase between the OEO and photonic link paths of 54° rather than 90° , which was required for the measurement.

5.5 Conclusions & Recommendations

The close-in RF phase noise of the OEO with RF phase noise cancellation (Fig. 5.3) was measured over a range of frequency offsets from 1 Hz to 1 MHz for both the OEO and photonic link sections comprising this structure. The phase noise of the OEO versus that of the photonic link was also measured over the same range of frequency offsets, but due to components being out of specification in the measurement setup, the collected data were unreliable and could not be processed.

As a result of components being out of specification in the measurement setup, it was not determined whether RF phase noise impressed on one laser wavelength could be used to cancel that on another laser wavelength to reduce the overall close-in phase noise in the RF domain.

Recommend redoing measurements with components that are within specification to determine whether close-in RF phase noise cancellation could be achieved.

Appendix A Instrumentation & Components

The laboratory instrumentation and link components that were used for these experiments are listed in Tables A.1-A.6. The specific setup in which the instruments and components were used is identified by the figure corresponding to the setup. The designator is the abbreviation, symbol, or word associated with the instrument or component on the figure.

Table A.1: Laboratory instrumentation used during experiment 1.

Instrument	Designator	Figure(s)	Make & Model
Electrical spectrum analyzer	ESA	3.1 & 3.2	Agilent PXA Signal Analyzer N9030A
Source meters	SMA & SMB	3.1	Keithley 2400 Source Meter
Power supplies	Not applicable	3.2	Agilent E3620A Dual Output DC Power Supply
Optical power meter	OPM	3.2	Newport Power Meter 2936-R
Optical power sensors	A & B	3.2	Newport Universal Fiber Optic Detector 918D-IS-IG

Table A.2: Laboratory instrumentation used during experiment 2.

Instrument	Designator	Figure(s)	Make & Model
RF oscillators	ψ_1 & ψ_2	4.1 & 4.2	PSI SLCO-BCS
Phase noise test set	ϕ NTS	4.1 & 4.2	Agilent E5500 A/B Phase Noise Test Set

Table A.3: Laboratory instrumentation used during experiment 3.

Instrument	Designator	Figure(s)	Make & Model
Electrical spectrum analyzer	ESA	5.1 & 5.2	Agilent PXA Signal Analyzer N9030A
RF oscillator	ψ	5.3	PSI SLCO-BCS
Low-phase noise arbitrary waveform generator	$L\phi$ N AWG	5.3	Keysight M8190A-LPN
Two channel digitizer	Digitizer	5.3	National Instruments PXI-5922

Table A.4: Link components used during experiment 1.

Component	Designator	Figure(s)	Make & Model
CW Laser	Laser	3.1 & 3.2	Gooch & Housego EM650
Mach-Zehnder modulator	Not applicable	3.2	EOSPACE AZ-1x2-AV5-40-PFA-PFA
Polarization maintaining fiber	PMF	3.1 & 3.2	FIS Simplex PM15U40 SM
Single-mode fiber	SMF	3.1 & 3.2	Corning SMF-28
Single-mode fiber spool	Test Spool 9.38953 km LEAF	3.1 & 3.2	Corning LEAF
Variable optical attenuator	VOA	3.1	EXFO FVA-600
Polarization controller	PC	3.1	THORLABS FPC560
Polarization beam splitter	PBS	3.1	OZ Optics FOBS-12P-111-9/125-PPS-1550-PBS-45
Variable optical delay line	VODL	3.1 & 3.2	General Photonics VDL-001-35-60-FC/APC-SS
Photodiodes A & B of balanced detector	PDA & PDB	3.1 & 3.2	Discovery Semiconductor DSC710-39-FC/UPC-K-1
Low noise amplifier	LNA	3.1 & 3.2	Miteq AU-1332
DC block	DCB	3.1 & 3.2	Tektronix PSPL550B
Bias tees	Not applicable	3.1 & 3.2	Picosecond Pulse Labs 5575A-104
Polarization maintaining isolator	PMI	3.2	Micro-Optics 1067
Farady rotating mirror	FRM	3.2	THORLABS MFI-1550-APC Inline Farady Rotator Mirror
Free-space polarization beam splitter	FSPBS	3.2	THORLABS FT-51X60
Optical couplers	98/2 OCA & 98/2 OCB	3.2	JDS Uniphase FFC-C2S21B110-003
Polarization maintaining optical coupler	50/50 PMOC	3.2	THORLABS 1550R5A2

Table A.5: Link components used during experiment 2.

Component	Designator	Figure(s)	Make & Model
CW Laser	Laser	4.1 & 4.2	
Bias control board	BCB	4.1 & 4.2	Pharad MBC-DF-UC-U Ultra-Compact Dither-Free Electro-Optic Modulator Bias Controller
Mach-Zehnder modulator	MZM	4.1 & 4.2	EOSPACE AZ-1x2-AV5-40-PFA-PFA
Variable optical attenuators	VOA1, VOA2, & VOA3	4.1 & 4.2	EXFO FVA-600
Single-mode fiber spools	SP1 & SP2	4.1 & 4.2	Corning SMF-28e
Erbium doped fiber amplifier	EDFA1 & EDFA2	4.1 & 4.2	Not available
Photodiode	PD	4.1	Not available
Photodiode	PD	4.2	Discovery Semiconductor DSC30S
Photodiode	PD	4.2	Discovery Semiconductor DSC50S
Dispersion compensating module	DCM 50 km	4.1	JDSU WRDCM-50
	DCM	4.2	JDSU WRDCM-50
Low-phase noise amplifier	LNA	4.1 & 4.2	Microsemi Corp AML812PNB1813
RF power divider	÷	4.2	Midwest Microwave PWD-5532-02-SMA-79

Table A.6: Link components used in experiment 3.

Component	Designator	Figure(s)	Make & Model
CW Laser	Laser	5.1 & 5.2	Gooch & Housego EM650
	Laser- λ_1	5.3	
	Laser- λ_2	5.3	
Bias control board	BCB	5.1 & 5.2	Pharad MBC-DF-UC-U Ultra-Compact Dither-Free Electro-Optic Modulator Bias Controller
	BCB1 & BCB2	5.3	
Mach-Zehnder modulator	MZM	5.1 & 5.2	EOSPACE AX-0MSS-20-PFA-SLA-LV
	MZM1	5.3	
	MZM2	5.3	
Variable optical attenuator	VOA	5.1, 5.2, & 5.3	EXFO FVA-600
Single-mode fiber spool	Test Spool 2 km SMF-28e	5.1 & 5.2	Corning SMF-28e
	Test Spool 5 km SMF-28e	5.3	
Photodiodes	PD	5.1 & 5.2	Discovery Semiconductor DSC30S
	PD1 & PD2	5.3	Discovery Semiconductor DSC50S
RF band pass filter	BPF	5.1 & 5.2	K&L Microwave 4C60-10240/T15-0/0
	BPF	5.3	K&L Microwave 5C45-2400/T10-0/0
Variable RF attenuator	VRA	5.1 & 5.2	Aeroflex/Weinschel AF117A-69-11
	VRA1 & VRA2	5.3	
Low noise amplifier	LNA	5.1 & 5.2	NDB C06018G-4F1
	LNA1 & LNA2	5.3	AML218P3401
RF phase shifter	$\Delta\Phi$	5.1 & 5.2	Sage 6705K-2
	$\Delta\Phi_a$ & $\Delta\Phi_b$	5.3	
RF power divider	\div	5.1, 5.2, & 5.3	Midwest Microwave PWD-5532-02-SMA-79
DC block	DCB	5.1 & 5.2	Tektronix PSPL550B
Bias tees	Not applicable	5.1, 5.2, & 5.3	Picosecond Pulse Labs 5575A-104
Fiber-optic circulator	FOC	5.2	JDS Fitel CR2500-4P
Farady rotating mirror	FRM	5.2	THORLABS MFI-1550-APC Inline Farady Rotator Mirror
Optical coupler	50/50 OC	5.3	Gould 450-000167
Wavelength division multiplexer/de-multiplexer	WDM/DEMUX	5.3	100G 1x16 DWDM Module
RF mixers	MIX1 & MIX2	5.3	Mini-Circuits (model not available)
RF hybrid coupler	RHC	5.3	Marki-Microwave (model not avail.)

Appendix B Calculation of DC Photocurrent

For the setup shown in Fig. 3.2, the measured optical power, responsivities of photodiodes A & B, and the coupling ratios of couplers A & B were used to calculate the photocurrent sourced by the photodiodes. A power balancing factor was also calculated and used to appropriately set the optical power incident on photodiodes A & B such that the DC photocurrents sourced by the photodiodes were equal in magnitude. Derivation of expressions used to calculate the DC photocurrent and the power balancing factor were obtained diagrammatically by using Fig. B.1 and are provided below. The inputs and outputs of the optical couplers shown in Fig. B.1 correspond to those shown in Fig. 3.2.



Fig. B.1: Diagram used to calculate and equalize photodiode A & B DC photocurrents. I₁ is the input to the coupler that was used, I₂ is the unused input, and O₁ and O₂ are the 98% and 2% outputs of the couplers, respectively. The 98% outputs were connected to the photodiodes and the 2% outputs were input to power sensors for measurement. The power from the 2% outputs was measured and used to determine the DC photocurrents.

The optical power emerging from output 1 of coupler A impinging on photodiode A is

$$P_{O1,A} = x_A P_{I1,A}, \quad (\text{B.1})$$

where x_A is ratio of the power emerging from output 1 of coupler A to that applied to input 1 of coupler A (~98%), and $P_{I1,A}$ is the optical power applied to input 1 of coupler A. Similarly, the optical power emerging from output 2 of coupler A that was input to power sensor A of the optical power meter for measurement is

$$P_{O2,A} = y_A P_{I1,A}, \quad (\text{B.2})$$

where y_A is the ratio of the power emerging from output 2 of coupler A to that applied to input 1 of coupler A (~2%). Solving Equations (B.1) and (B.2) for $P_{I1,A}$, equating, and rearranging yields the optical power incident on photodiode A in terms of that measured from output 2 of coupler A and the coupling ratios:

$$P_{O1,A} = \frac{x_A}{y_A} P_{O2,A}. \quad (\text{B.3})$$

The magnitude of the DC photocurrent sourced by photodiode A is

$$|I_{dc,A}| = |R_A| P_{O1,A}, \quad (\text{B.4})$$

where $|R_A|$ is the magnitude of the responsivity of photodiode A. The photocurrent sourced by photodiode A, $I_{dc,A}$, is positive. By inserting Equation (B.3) into Equation (B.4), the magnitude of the DC photocurrent generated by photodiode A in terms of the coupling ratios and the optical power measured from output 2 of coupler A is found to be

$$|I_{dc,A}| = |R_A| \frac{x_A}{y_A} P_{O2,A}. \quad (B.5)$$

Expressions similar to those derived in Equations (B.1)-(B.5) for coupler A can be derived for coupler B. The magnitude of the DC photocurrent produced by photodiode B in terms of the coupling ratios, x_B and y_B , and the optical power measured by the optical power meter and power sensor B connected to output 2 of coupler B, $P_{O2,B}$, is

$$|I_{dc,B}| = |R_B| \frac{x_B}{y_B} P_{O2,B}, \quad (B.6)$$

where $|R_B|$ is the magnitude of the responsivity of photodiode B. The photocurrent sourced by photodiode B, $I_{dc,B}$, is negative. Realizing that for balanced detection $|I_{dc,A}| = |I_{dc,B}|$, equating Equations (B.5) and (B.6) and solving for the optical power emerging from output 2 of coupler A in terms of that emerging from output 2 of coupler B yields

$$P_{O2,A} = \frac{|R_B| y_A x_B}{|R_A| x_A y_B} P_{O2,B}, \quad (B.7)$$

where the factor relating the optical power levels emerging from output 2 of couplers A and B was used to balance the photocurrents, $I_{dc,A}$ and $I_{dc,B}$, and is defined as

$$B \equiv \frac{|R_B| y_A x_B}{|R_A| x_A y_B}. \quad (B.8)$$

Inserting (B.8) into (B.7) and expressing the power balancing factor in terms of the power emerging from output 2 of couplers A and B yields

$$B = \frac{P_{O2,A}}{P_{O2,B}}. \quad (B.9)$$

In decibel form, Equation (B.9) is

$$B[dB] = P_{O2,A}[dBm] - P_{O2,B}[dBm]. \quad (B.10)$$

Equation (B.10) is the relationship that was used to appropriately set the measured power levels emerging from output 2 of couplers A and B relative to one another, along with the power levels incident on photodiodes A and B, to achieve equal magnitude DC photocurrents sourced by photodiodes A and B.

Appendix C Output Noise Power Spectral Density & Relative Intensity Noise

Appendix C.1 Noise Power Spectral Density Plots

Plots showing the measured single-sided output noise power spectral density of the links utilizing polarization multiplexing/de-multiplexing and balanced detection (Fig. 3.1) plus retroreflection (Fig. 3.2) are provided in Figs. C.1-C.4. Figs. C.1-C.2 show the output noise power spectral density of the entire link (optical section plus RF section) and just the optical section, respectively, for the link in Fig 3.1. Similarly, Figs. C.3-C.4 show the output noise power spectral density of the whole link and that of only the optical section, respectively, for the link in Fig. 3.2.

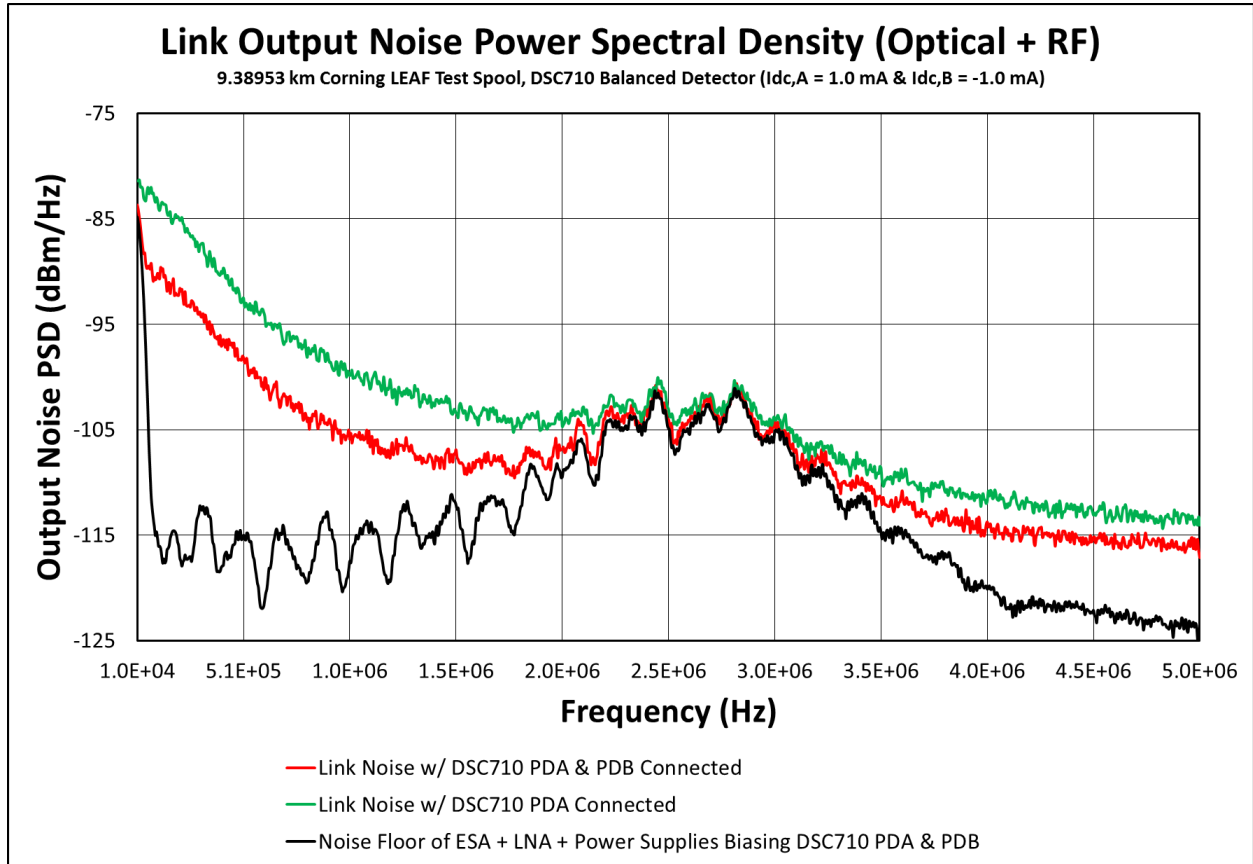


Fig. C.1: Single-sided output noise power spectral density (PSD) for entire link utilizing polarization multiplexing/de-multiplexing and balanced detection to reduce noise due to DRS.

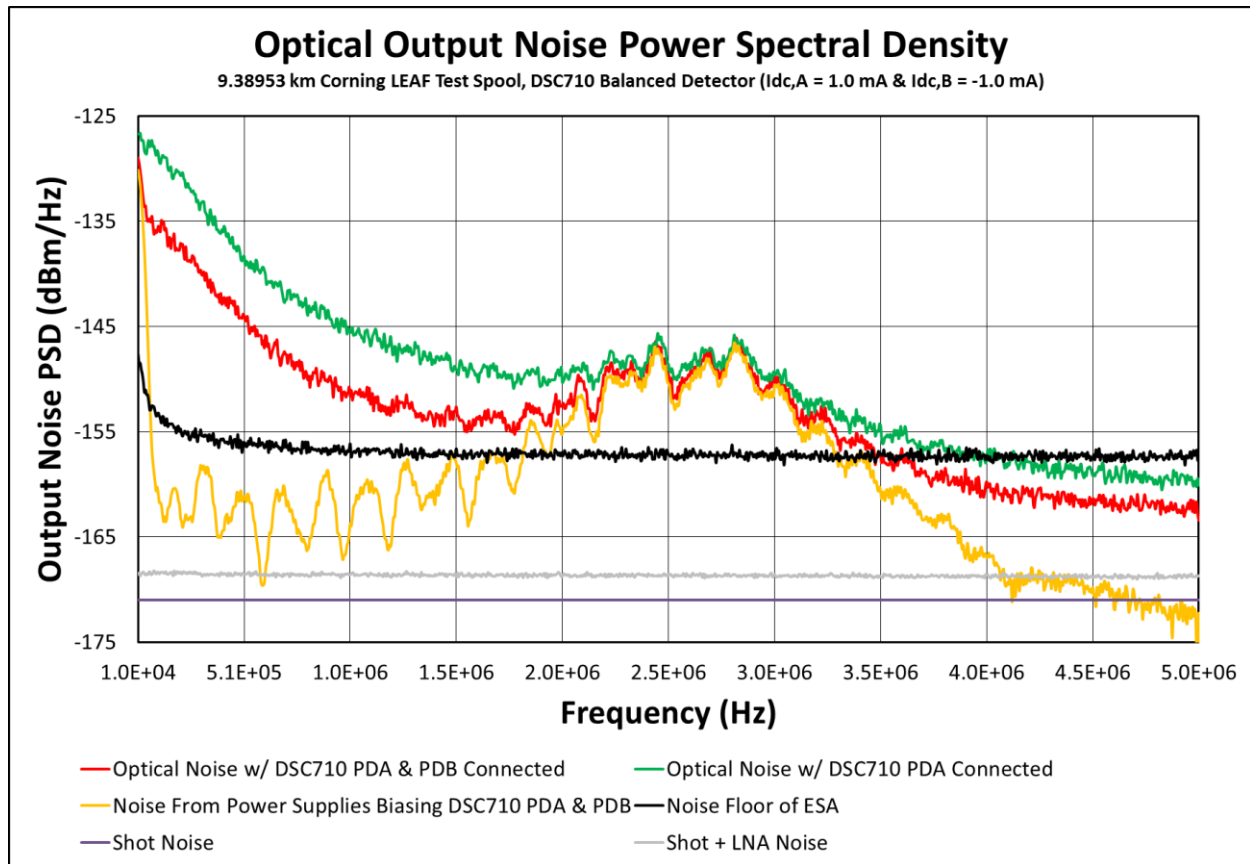


Fig. C.2: Single-sided output noise power spectral density (PSD) for optical section of link utilizing polarization multiplexing/de-multiplexing and balanced detection to reduce noise due to DRS.

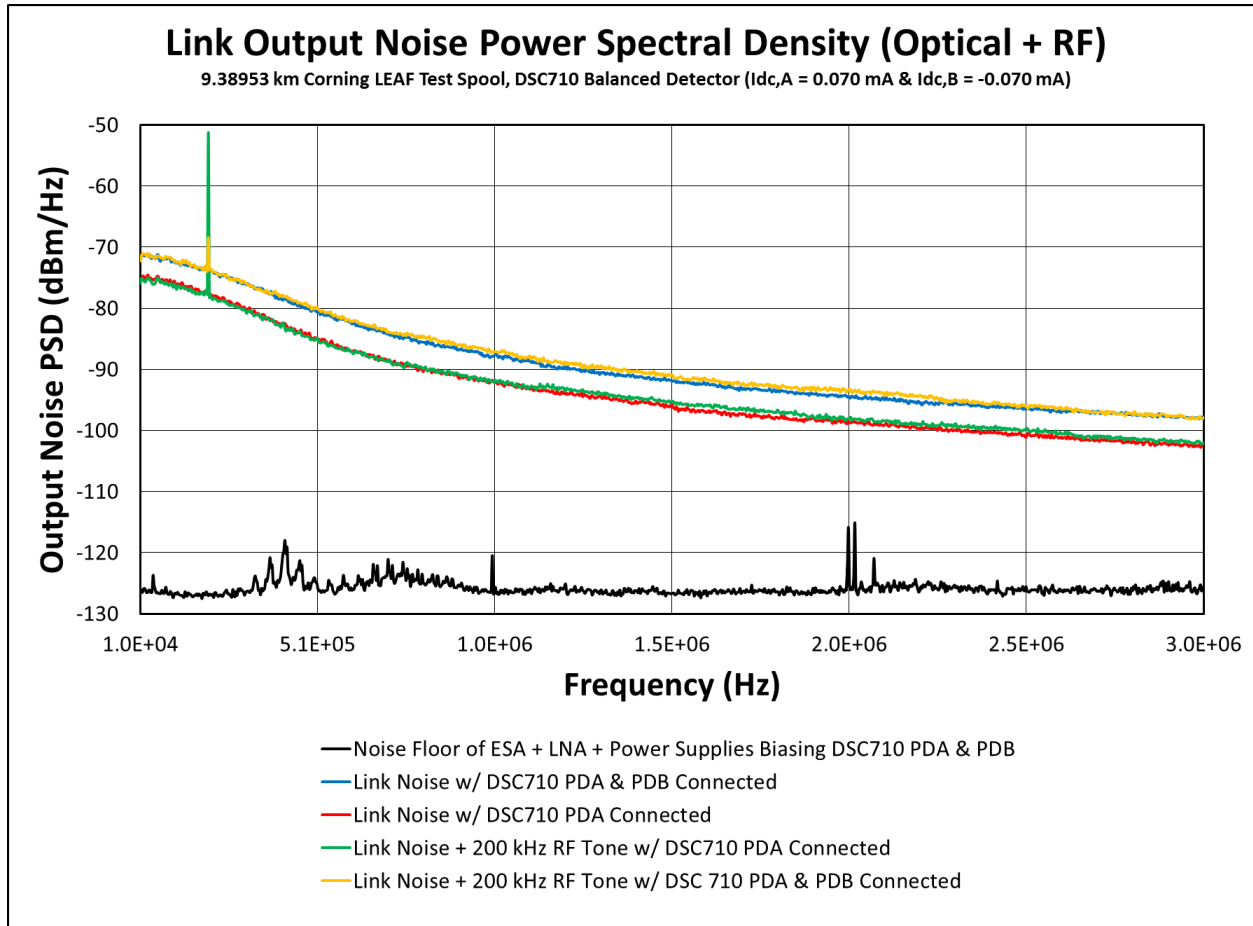


Fig. C.3: Single-sided output noise power spectral density (PSD) for entire link utilizing polarization multiplexing/de-multiplexing, balanced detection, and retroreflection to address noise due to DRS.

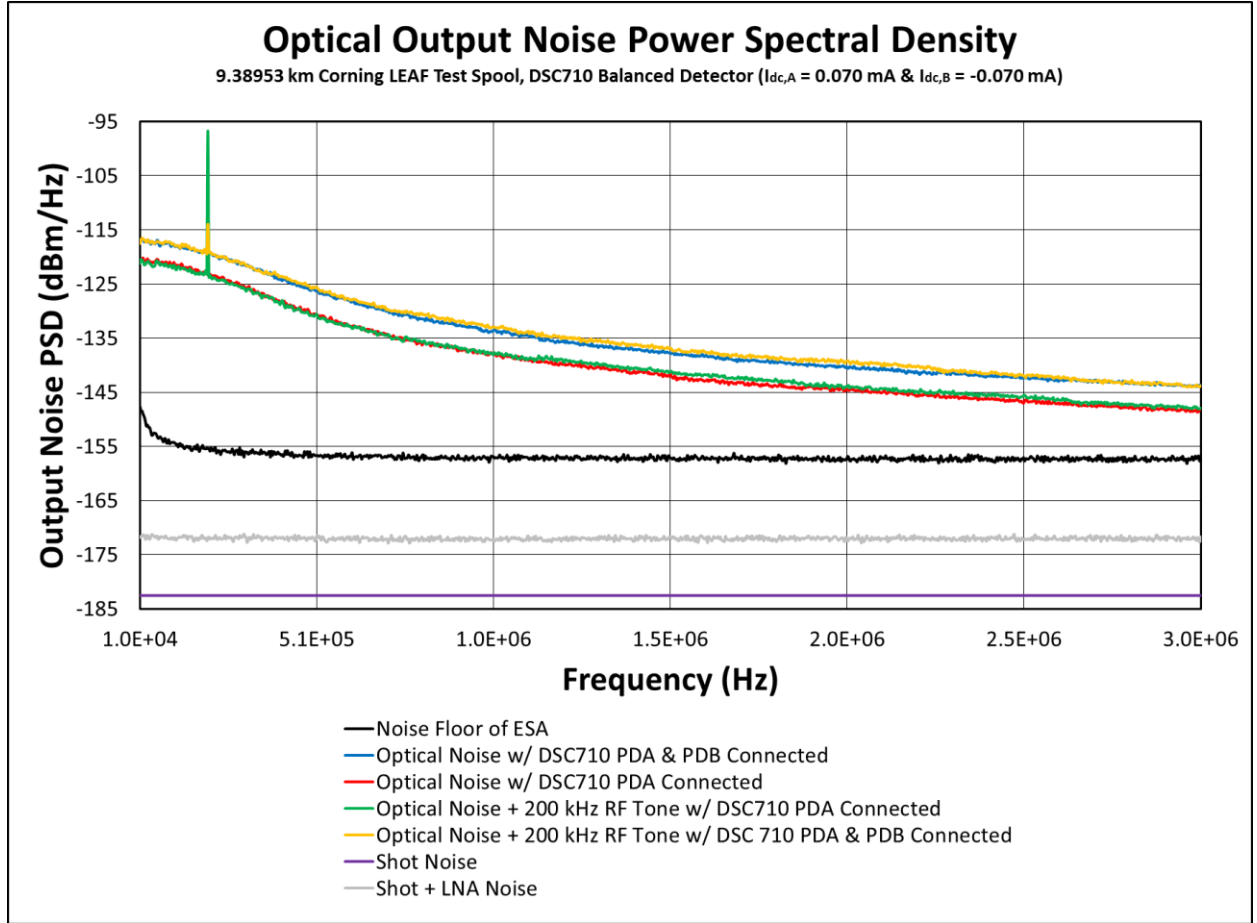


Fig. C.4: Single-sided output noise power spectral density (PSD) for optical section of link utilizing polarization multiplexing/de-multiplexing, balanced detection, and retroreflection to address noise due to DRS.

Appendix C.2 Noise Power Spectral Density & Relative Intensity Noise Calculations

The single-sided output noise power spectral density due to shot noise generated during optical-to-electrical conversion was obtained using

$$N_{Sh}[mW/Hz] = 2qI_{dc}R|H_{pd}|^2, \quad (C.1)$$

where q is the elementary charge constant, I_{dc} is the DC photocurrent, R is the load resistance (50Ω), and H_{pd} is the photodiode filter function ($1/2$). Expressed in decibel form, Equation (C.1) becomes

$$N_{Sh}[dBm/Hz] = -168 + 10 \log(I_{dc}[mA]) + 2H_{pd}[dB]. \quad (C.2)$$

Equation (C.2) was used to produce the single-sided output noise power spectral density shot noise curves shown in Figs. C.2 and C.4.

The single-sided output noise power spectral density due to superposed shot and LNA noise was obtained using

$$N_{Sh+LNA}[mW/Hz] = N_{Sh}[mW/Hz] + \frac{N_{LNA}}{g_{LNA}}, \quad (C.3)$$

where N_{LNA} is the output noise power spectral density of the LNA and g_{LNA} is the small-signal RF gain of the LNA. Equation (C.3) expressed in decibel form is

$$N_{Sh+LNA}[dBm/Hz] = N_{Sh}[dBm/Hz] + N_{LNA}[dBm/Hz] - G_{LNA}[dB]. \quad (C.4)$$

Equation (C.4) was used to generate the single-sided output noise power spectral density shot plus LNA noise curves shown in Figs. C.2 and C.4.

The single-sided output noise power spectral density curves displayed in Figs. C.2 and C.4 for the ESA were obtained by measuring the noise floor of the ESA, with its input terminated in an impedance matched 50 Ω load, and normalizing to a 1 Hz bandwidth, a calculation of which is shown in decibel form as

$$N_{ESA}[dBm/Hz] = P_{RF,ESA}[dBm] - 10 \log(RBW_{ESA}[Hz]), \quad (C.5)$$

where $P_{RF,ESA}$ is the noise floor of the ESA and RBW_{ESA} is the resolution bandwidth of the ESA.

An expression similar to that given in Equation (C.5) was used to produce the single-sided output noise power spectral density curves in Figs. C.1 and C.3 for the superposed ESA, power supply, and LNA noise

$$N_{ESA+PS+LNA}[dBm/Hz] = P_{RF,ESA+PS+LNA}[dBm] - 10 \log(RBW_{ESA}[Hz]), \quad (C.6)$$

where $P_{RF,ESA+PS+LNA}$ is the measured RF output power due to the noise from the ESA, power supplies, and LNA.

The single-sided output noise power spectral density curves displayed in Figs. C.1 and C.3 for the entire link were obtained by measuring RF output power and normalizing to a 1 Hz bandwidth, a calculation of which is shown in decibel form as

$$N_{Link}[dBm/Hz] = P_{RF,Link}[dBm] - 10 \log(RBW_{ESA}[Hz]), \quad (C.7)$$

where $P_{RF,Link}$ is the measured RF output power of the link.

The single-sided output noise power spectral density of the power supplies used to bias the photodiodes was obtained by removing the single-sided output noise power spectral density of the RF section, specifically that of the LNA, and is given as

$$N_{PS}[mW/Hz] = \frac{N_{ESA+PS+LNA}}{g_{LNA}} - \frac{N_{LNA}}{g_{LNA}}. \quad (C.8)$$

Expressed in decibel form, Equation (C.8) becomes

$$N_{PS}[dBm/Hz] = 10\log(N_{ESA+PS+LNA}[mW/Hz] - N_{LNA}[mW/Hz]) - G_{LNA}[dB]. \quad (C.9)$$

Equation (C.9) was used to produce the single-sided output noise power spectral density curve displayed on Fig. C.2 for the power supplies used to bias the photodiodes.

Similarly, the single-sided output noise power spectral density of just the optical portion of the link was obtained by removing the single-sided output noise power spectral density of the LNA and is given as

$$N_{opt}[mW/Hz] = \frac{N_{Link}}{g_{LNA}} - \frac{N_{LNA}}{g_{LNA}}. \quad (C.10)$$

Expressed in decibel form, Equation (C.10) becomes

$$N_{opt}[dBm/Hz] = 10\log(N_{Link}[mW/Hz] - N_{LNA}[mW/Hz]) - G_{LNA}[dB]. \quad (C.11)$$

Equation (C.11) was used to produce the single-sided output noise power spectral density curves displayed in Figs. C.2 and C.4 for the optical portion of the link.

Noise due to optical intensity fluctuations relative to the optical carrier, which manifests in the RF domain upon photodetection, is given by

$$RIN = \frac{N_{opt}B}{I_{dc}^2 R |H_{pd}|^2}, \quad (C.12)$$

where B is the normalized 1 Hz bandwidth. Equation (C.12) can be expressed in decibel form as

$$RIN[dBc/Hz] = 13 + N_{opt}[dBm/Hz] - 20\log(I_{dc}[mA]) - 2H_{pd}[dB]. \quad (C.13)$$

Equation (C.11) was inserted into Equation (C.13) to produce the optical RIN curves shown in Figs. 3.3-3.4. The single-sided output noise power spectral density values given by Equations (C.2), (C.4), (C.5), and (C.9) were also inserted into Equation (C.13) to generate the RIN curves for shot noise, superposed shot and LNA noise, the noise floor of the ESA, and power supply noise, respectively. RIN is typically reserved for quantifying noise that originates in the optical domain; however, the electrical noise generated by the ESA, LNA, and power supplies was converted to RIN so that it could be directly compared to the other sources of noise due to optical intensity fluctuations.

References

- [1] Thorlabs, Inc., https://www.thorlabs.com/newgrouppage9.cfm?objectgroup_id=3365.
- [2] V. J. Urick, J. D. McKinney, and K. J. Williams, *Fundamentals of Microwave Photonics*, Wiley, 2015.
- [3] V. J. Urick, M. N. Hutchinson, R. T. Schermer, “Investigation of analog photonic link technology for timing and metrological applications,” Naval Research Laboratory Memorandum Report, NRL/MR/5650-15-9626, May 2015.
- [4] Agilent, “Agilent E5500 series phase noise measurement solutions data sheet,” July 2014.

